Roughness-induced superhydrophobicity: a way to design non-adhesive surfaces

2008 J. Phys.: Condens. Matter 20 225009

(http://iopscience.iop.org/0953-8984/20/22/225009)

IOP PUBLISHING JOURNAL OF PHYSICS: CONDENSED MATTER

J. Phys.: Condens. Matter **20** (2008) 225009 (30pp) doi:10.1088/0953-8984/20/22/225009

Roughness-induced superhydrophobicity: a way to design non-adhesive surfaces

Michael Nosonovsky[1] **and Bharat Bhushan**[2,3]

[1] National Institute of Standards and Technology, 100 Bureau Drive, Stop 8520, Gaithersburg, MD 20899-8520, USA
[2] Nanotribology Laboratory for Information Storage and MEMS/NEMS(NLIM), The Ohio State University, 201 West 19th Avenue, Columbus, OH 43210-1142, USA

E-mail: bhushan.2@osu.edu

Received 31 July 2007
Published 30 April 2008
Online at stacks.iop.org/JPhysCM/20/225009

Abstract

Non-adhesive and water-repellent surfaces are required for many tribological applications. Roughness-induced superhydrophobicity has been suggested as a way to reduce adhesion and stiction. In this paper, the theory of roughness-induced superhydrophobicity is presented. Wetting is studied as a multiscale process involving the macroscale (water droplet size), microscale (surface texture size), and nanoscale (molecular size). We study fundamental physical mechanisms of wetting, including the transition between various wetting regimes, contact angle and contact angle hysteresis. The effect of surface roughness upon wetting and capillary adhesion force is discussed. Practical recommendations for the design of superhydrophobic surfaces are formulated.

(Some figures in this article are in colour only in the electronic version)

1. Introduction

Numerous micro/nanotribological and micro/nanomechanical applications, such as the micro/nanoelectromechanical systems (MEMS/NEMS), require surfaces with low adhesion and stiction (Bhushan *et al* 1995, Bhushan 1998, 2003, 2007). As the size of these devices decreases, the surface forces tend to dominate over the volume forces, and adhesion and stiction constitute a challenging problem for proper operation of these devices. This makes the development of non-adhesive surfaces crucial for many of these emerging applications. It has been suggested that extremely water-repellent (superhydrophobic) surfaces produced by applying a micropatterned roughness combined with hydrophobic coatings may satisfy the need for the non-adhesive surfaces (Nosonovsky and Bhushan 2005, 2006a, 2006b, 2007a, 2007b, Bhushan *et al* 2007). Wetting may lead to the formation of menisci at the interface between solid bodies during sliding contact, which increases adhesion/friction. As a result of this, the wet friction force is greater than the dry friction force, which is usually undesirable (Bhushan 1999, 2002, 2005). On the other hand, high adhesion is desirable in some applications, such as adhesive tapes and the adhesion of cells to biomaterial surfaces, therefore, enhanced wetting by changing roughness would be desirable in these applications (Nosonovsky and Bhushan 2005, 2006a).

The primary parameter that characterizes wetting is the static contact angle, which is defined as the measurable angle which a liquid makes with a solid. The contact angle depends on several factors, such as roughness and the manner of surface preparation and its cleanliness (Adamson 1990, Israelachvili 1992). If the liquid wets the surface (referred to as a wetting liquid or a hydrophilic surface), the value of the static contact angle is $0° \leqslant \theta \leqslant 90°$, whereas if the liquid does not wet the surface (referred to as a non-wetting liquid or a hydrophobic surface), the value of the contact angle is $90° < \theta \leqslant 180°$. The term hydrophobic/-philic, which was originally applied only to water ('hydro' means 'water' in Greek), is often used to describe the contact of a solid surface with any liquid. The term 'oleophobic/-philic' is sometimes used with regard to the wetting by oil. Surfaces with high energy, formed by polar molecules, tend to be hydrophilic, whereas those with low energy and built of non-polar molecules tend to be hydrophilic.

Surfaces with a contact angle between 150° and 180° are called superhydrophobic. For liquid flow applications, in addition to high contact angle, superhydrophobic surfaces also have very low water contact angle hysteresis. The contact

[3] Author to whom any correspondence should be addressed.

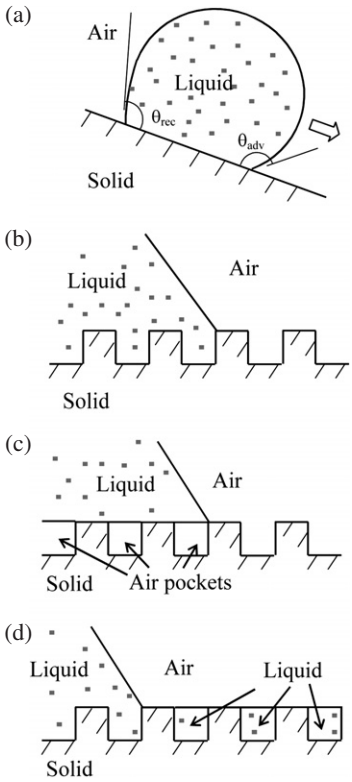

Figure 1. (a) Schematics of a droplet on a tilted substrate showing advancing (θ_{adv}) and receding (θ_{rec}) contact angles. The difference between these angles constitutes the contact angle hysteresis. Configurations described by the Wenzel equation for the homogeneous interface (equation (1)), (b) the Cassie–Baxter equation for the composite interface with air pockets (equation (3)), and (c) the Cassie equation for the homogeneous interface (equation (4)).

angle hysteresis is the difference between the advancing and receding contact angles, which are two stable values. If additional liquid is added to a sessile drop the contact line advances, and each time motion ceases the drop exhibits an advancing contact angle. Alternatively, if liquid is removed from the drop the contact angle decreases to a receding value before the contact retreats. For a droplet moving along the solid surface (for example, if the surface is tilted) there is another definition. The contact angle at the front of the droplet (advancing contact angle) is greater than that at the back of the droplet (receding contact angle), due to roughness, resulting in the contact angle hysteresis (figure 1(a)). It has been disputed that the two definitions are equivalent (Krasovitski and Marmur 2004); however, in many cases the two definitions have the same meaning. Surfaces with low contact angle hysteresis have a very low water roll-off angle which denotes the angle to which a surface must be tilted for roll off of water drops (i.e. very low water contact angle hysteresis) (Extrand 2002, Kijlstra *et al* 2002).

One of the ways to increase the hydrophobic or hydrophilic properties of the surface is to increase surface roughness, so roughness-induced hydrophobicity has become a subject of extensive investigation. Wenzel (1936) found that the contact angle of a liquid with a rough surface is different from that with a smooth surface. Cassie and Baxter (1944) showed that air (or gas) pockets may be trapped in the cavities of a rough surface, resulting in a composite solid–liquid–air interface, as opposed to a homogeneous solid–liquid interface. Shuttleworth and Bailey (1948) studied spreading of a liquid over a rough solid surface and found that the contact angle at the absolute minimum of surface energy corresponds to the values predicted by Wenzel (1936) or Cassie and Baxter (1944). Johnson and Dettre (1964) showed that the homogeneous and composite interfaces correspond to the two metastable equilibrium states of a droplet. Bico *et al* (2002), Marmur (2003, 2004), Lafuma and Quéré (2003), Patankar (2003, 2004a), He *et al* (2003) and other authors recently investigated the metastability of artificial superhydrophobic surfaces and showed that whether the interface is homogeneous or composite may depend on the history of the system (in particular, whether the liquid was applied from the top or from the bottom). Extrand (2002) pointed out that whether the interface is homogeneous or composite depends on droplet size, due to gravity. It was suggested also that the so-called two-tiered (or double) roughness, made up of superposition of two roughness patterns at different length-scales (Herminghaus 2000, Patankar 2004b, Sun *et al* 2005), and fractal roughness (Shibuichi *et al* 1996) may lead to superhydrophobicity. Herminghaus (2000) showed that certain self-affine profiles may result in superhydrophobic surfaces even for wetting liquids, in the case the local equilibrium condition for the triple line (line of contact between solid, liquid and air) is satisfied. Nosonovsky and Bhushan (2005, 2006a) pointed out that such configurations, although formally possible, are likely to be unstable. Nosonovsky and Bhushan (2006a, 2006b) proposed a stochastic model for wetting of rough surfaces with a certain probability associated with every equilibrium state. According to their model, the overall contact angle with a two-dimensional rough profile is calculated by assuming that the overall configuration of a droplet occurs as a result of superposition of numerous metastable states. The probability-based concept is consistent with the experimental data (Lafuma and Quéré 2003), which suggest that transition between the composite and homogeneous interfaces is gradual rather than instant.

It has been demonstrated experimentally that roughness changes the contact angle in accordance with the Wenzel model. Yost *et al* (1995) found that roughness enhances wetting of a copper surface with Sn–Pb eutectic solder, which has a contact angle of 15°–20° for a smooth surface. Shibuichi *et al* (1996) measured the contact angle of various liquids (mixtures of water and 1,4-dioxane) on alkylketene dimer (AKD) substrate (contact angle not larger than 109° for a smooth surface). They found that for wetting liquids the contact angle decreases with increasing roughness, whereas for non-wetting liquids it increases. Semal *et al* (1999) investigated the effect of surface roughness on contact angle hysteresis by studying a sessile droplet of squalane spreading dynamically on multilayer substrates (behenic acid on glass) and found that an increase in microroughness slows the rate of droplet spreading. Erbil *et al* (2003) measured the contact angle of polypropylene (contact angle of 104° for a smooth

surface) and found that the contact angle increases with increasing roughness. Burton and Bhushan (2005) measured contact angle with roughness of patterned surfaces and found that in the case of hydrophilic surfaces it decreases with increasing roughness, and for hydrophobic surfaces it increases with increasing roughness. Jung and Bhushan (2006, 2007) and Bhushan and Jung (2007) studied the wetting properties of hydrophobic and hydrophilic leafs and patterned surfaces and found similar trends.

In the last decade, material scientists have given attention to natural surfaces that are extremely hydrophobic. Among them are the leaves of water-repellent plants such as *Nelumbo nucifera* (lotus) and *Colocasia esculenta*, which have high contact angles with water (Neinhuis and Barthlott 1997, Barthlott and Neinhuis 1997, Wagner *et al* 2003). First, the surface of the leaves is usually covered with a range of different waxes made from a mixture of hydrocarbon compounds that have are strongly hydrophobic. Second, the surface is very rough due to so-called papillose epidermal cells which form asperities or papillae. In addition to the microscale roughness of the leaf due to the papillae, the surface of the papillae is also rough with submicron sized asperities composed of the wax (Wagner *et al* 2003). Thus they have hierarchical micro- and nanosized structures, which have been studied extensively by Bhushan and Jung (2006). The water droplets on these surfaces readily sit on the apex of nanostructures because air bubbles fill in the valleys of the structure under the droplet. Therefore, these leaves exhibit considerable superhydrophobicity. The water droplets on the leaves remove any contaminant particles from the surfaces when they roll off, leading to a self cleaning ability referred to as the lotus-effect. Other examples of biological surfaces include duck feathers and butterfly wings. Their corrugated surfaces provide air pockets that prevent water from completely touching the surface. Study and simulation of biological objects with desired properties is referred to as 'biomimetics', which comes from a Greek word 'biomimesis' meaning to mimic life.

As far as the realization of strongly water-repellent artificial surfaces is concerned, they can be constructed by chemically treating surfaces with low-surface-energy substances such as polytetrafluoroethylene, silicon, or wax, or by fabricating extremely rough hydrophobic surfaces directly (Shibuichi *et al* 1996, Miwa *et al* 2000, He *et al* 2003, Kijlstra *et al* 2002). Sun *et al* (2005) studied an artificial poly(dimethylsiloxane) (PDMS) replica of the surface of a lotus leaf and found a water contact angle of 160° for the rough surface, whereas for the smooth PDMS surface it is about 105°.

As stated earlier, when two solids come in contact in the presence of a wetting liquid, a meniscus is often formed (Bhushan 1999, 2002, 2003, 2005). A meniscus results in the normal meniscus force, which, in turn, results in an increase in the tangential friction force. The magnitude of the meniscus force depends on the number of asperity contacts and asperity radii, which depend on roughness, and on surface tension of the liquid and the contact angle. The contact angle, as stated above, depends on surface roughness, and thus roughness affects the wet friction force (Nosonovsky and Bhushan 2005). In the present paper we will discuss the contact angle and contact angle hysteresis of a liquid droplet upon rough surfaces, as well as stability and the transition between wetting regimes. The effect of roughness upon the adhesion force will also be discussed.

2. Contact angle analysis

In this section, the dependence of the contact angle on the surface tension is considered for a liquid in contact with a smooth and a rough solid surface, forming a homogeneous interface. The surface atoms or molecules of liquids or solids have energy above that of similar atoms and molecules in the interior, which results in surface tension or free surface energy being an important surface property. This property is characterized quantitatively by the surface tension or free surface energy γ, which is equal to work that is required to create a unit area of the surface at constant volume and temperature. The units of γ are J m^{-2} or N m^{-1} and it can be interpreted either as energy per unit surface area or as tension force per unit length of a line at the surface. When a solid is in contact with liquid, the molecular attraction will reduce the energy of the system below that for the two separated surfaces. This may be expressed by the Dupré equation

$$W_{\mathrm{SL}} = \gamma_{\mathrm{SA}} + \gamma_{\mathrm{LA}} - \gamma_{\mathrm{SL}} \tag{1}$$

where W_{SL} is the work of cohesion per unit area between two surfaces, γ_{SA} and γ_{SL} are the surface energies (surface tensions) of the solid against air and liquid, and γ_{LA} is the surface energy (surface tension) of liquid against air (Israelachvili 1992).

If a droplet of liquid is placed on a solid surface, the liquid and solid surfaces come together under equilibrium at a characteristic angle called the static contact angle θ_0. This contact angle can be determined from the condition of the net free surface energy of the system being minimized (Adamson 1990, Israelachvili 1992). The total energy E_{tot} is given by

$$E_{\mathrm{tot}} = \gamma_{\mathrm{LA}}(A_{\mathrm{LA}} + A_{\mathrm{SL}}) - W_{\mathrm{SL}}A_{\mathrm{SL}} \tag{2}$$

where A_{LA} and A_{SL} are the contact areas of the liquid with the solid and air, respectively. It is assumed that the droplet is small enough so that the gravitational potential energy can be neglected. It is also assumed that the volume and pressure are constant, so that the volumetric energy does not change. At the equilibrium $\mathrm{d}E_{\mathrm{tot}} = 0$, which yields

$$\gamma_{\mathrm{LA}}(\mathrm{d}A_{\mathrm{LA}} + \mathrm{d}A_{\mathrm{SL}}) - W_{\mathrm{SL}}\mathrm{d}A_{\mathrm{SL}} = 0. \tag{3}$$

For a droplet of constant volume it is easy to show, using geometrical considerations, that

$$\mathrm{d}A_{\mathrm{LA}}/\mathrm{d}A_{\mathrm{SL}} = \cos\theta_0. \tag{4}$$

Combining equations (1), (3), and (4), the well-known Young equation for the contact angle is obtained:

$$\cos\theta_0 = \frac{\gamma_{\mathrm{SA}} - \gamma_{\mathrm{SL}}}{\gamma_{\mathrm{LA}}}. \tag{5}$$

Equation (5) provides us with the value of the static contact angle for given surface tensions. Note that although we use the term 'air', the analysis does not change in the case of another gas, such as a liquid vapor.

3. Heterogeneous surfaces and the Wenzel and Cassie equations

In this section, we will discuss the so-called heterogeneous interface and introduce the equations that govern the contact angle for the heterogeneous interface.

3.1. Contact angle with rough and heterogeneous surfaces

The Wenzel (1936) equation, which was derived using the surface force balance and empirical considerations, relates the contact angle of a water droplet upon a rough solid surface, θ, with that upon a smooth surface, θ_0 (figure 1(b)), through the non-dimensional surface roughness factor, R_f, equal to the ratio of the surface area to its flat projection

$$\cos\theta = \frac{dA_{LA}}{dA_F} = \frac{dA_{SL}}{dA_F}\frac{dA_{LA}}{dA_{SL}} = R_f \cos\theta_0 \tag{6}$$

$$R_f = \frac{A_{SL}}{A_F}. \tag{7}$$

In a similar manner, for a surface composed of two fractions, one with fractional area f_1 and contact angle θ_1 and the other with f_2 and θ_2, respectively (so that $f_1 + f_2 = 1$), the contact angle is given by the Cassie equation

$$\cos\theta = f_1 \cos\theta_1 + f_2 \cos\theta_2. \tag{8}$$

For the case of a composite interface (figure 1(c)), consisting of the solid–liquid fraction ($f_1 = f_{SL}$, $\theta_1 = \theta_0$) and liquid–vapor fraction ($f_2 = 1 - f_{SL}$, $\cos\theta_2 = -1$), combining the equations (7) and (8) yields the Cassie–Baxter equation

$$\cos\theta = R_f f_{SL} \cos\theta_0 - 1 + f_{SL}. \tag{9}$$

The opposite limiting case of $\cos\theta_2 = 1$ ($\theta_2 = 0°$ corresponds to water-on-water contact) yields

$$\cos\theta = 1 + f_{SL}(\cos\theta_0 - 1). \tag{10}$$

Equation (10) is sometimes used (de Gennes *et al* 2003) for the homogeneous interface instead of equation (6) if the rough surface is covered by holes filled with water (figure 1(d)).

3.2. The Cassie–Baxter equation

Two situations in wetting of a rough surface should be distinguished: a homogeneous interface without any air pockets (sometimes called a Wenzel interface, since the contact angle is given by the Wenzel equation or equation (6)) and a composite interface with air pockets trapped between the rough details (sometimes called a Cassie or Cassie–Baxter interface, since the contact angle is given by equation (9)). While equation (9) for a composite interface can be derived using equations (6) and (8), it can also be obtained independently. For this purpose, two sets of interfaces are considered: a liquid–air interface with the ambient and a flat composite interface under the droplet, which itself involves solid–liquid, liquid–air, and solid–air interfaces. For fractional flat geometrical areas of the solid–liquid and liquid–air interfaces under the droplet, f_{SL} and f_{LA}, the flat area of the composite interface is

$$A_C = f_{SL}A_C + f_{LA}A_C = R_f A_{SL} + f_{LA}A_C. \tag{11}$$

In order to calculate the contact angle in a manner similar to the derivation of equation (6), the differential area of the liquid–air interface under the droplet, $f_{LA}\,dA_C$, should be subtracted from the differential of the total liquid–air area dA_{LA}, which yields

$$\cos\theta = \frac{dA_{LA} - f_{LA}dA_C}{dA_C} = \frac{dA_{SL}}{dA_F}\frac{dA_F}{dA_C}\frac{dA_{LA}}{dA_{SL}} - f_{LA} = R_f f_{SL}\cos\theta_0 - f_{LA}. \tag{12}$$

According to equation (12) (which is equivalent to equation (9)) in the limit of high R_f, f_{SL} approaches zero, whereas f_{LA} approaches unity, and hence θ approaches 180°. However, the Cassie–Baxter model does not provide any particular form of dependence of f_{SL} and f_{LA} on R_f and does not explain under which conditions the composite interface forms.

Shuttleworth and Bailey (1948) studied spreading of a liquid over a rough solid surface and found that the contact angle at the absolute minimum of surface energy corresponds to the values given by equation (6) (for a homogeneous interface) or equation (12) (for a composite interface). According to their analysis, spreading of a liquid continues until simultaneously equation (5) (the Young equation) is satisfied locally at the triple line and the minimal surface condition is satisfied over the entire liquid–air interface. The minimal surface condition states that the sum of the inverse principal radii of curvature, R_1 and R_2, is constant at any point, and thus governs the shape of the liquid–air interface.

$$\frac{1}{R_1} + \frac{1}{R_2} = \text{const.} \tag{13}$$

Johnson and Dettre (1964) showed that the homogeneous and composite interfaces correspond to the two stable or metastable states of a droplet. Even though it may be geometrically possible for the system to become composite, it may be energetically profitable for the liquid to penetrate into valleys between asperities and to form a homogeneous interface. Marmur (2003) formulated the geometrical conditions for a surface under which the energy of the system has a local minimum and the composite interface may exist. Patankar (2004a) pointed out that whether a homogeneous or composite interface exists depends on the system's history, i.e. on whether the droplet was formed at the surface or deposited. However, the above-mentioned analyses do not provide us with the answer of which of the two possible configurations, homogeneous or composite, will actually form.

3.3. Limitations of the Wenzel and Cassie equations

The Cassie equation (equation (8)) is based on the assumption that the heterogeneous surface is composed of well-separated distinct patches of different material, so that the free surface energy can be averaged. It has been argued also that when the size of the chemical heterogeneities is very small (of atomic or molecular dimensions), the quantity that should be averaged

Table 1. Wetting of a superhydrophobic surface as a multiscale process.

Scale level	Characteristic length	Parameters	Phenomena	Interface
Macroscale	Droplet radius (mm)	Contact angle, droplet radius	Contact angle hysteresis	2D
Microscale	Roughness detail (μm)	Shape of the droplet, position of the liquid–vapor interface (h)	Kinetic effects	3D solid surface, 2D liquid surface
Nanoscale	Molecular heterogeneity (nm)	Molecular description	Thermodynamic and dynamic effects	3D

is not the energy but the dipole moment of a macromolecule (Israelachvili and Gee 1989), and equation (8) should be replaced by

$$(1+\cos\theta)^2 = f_1(1+\cos\theta_1)^2 + f_2(1+\cos\theta_2)^2. \qquad (14)$$

Experimental studies of polymers with different functional groups showed a good agreement with equation (14) (Tretinnikov 2000).

Later investigations put the Wenzel and Cassie equations into a thermodynamic framework; however, they also showed that there is no one single value of the contact angle for a rough or heterogeneous surface (Johnson and Dettre 1964, Marmur 2003, Li and Amirfazli 2006). The contact angle can be in a range of values between the so-called receding contact angle, θ_{rec}, and the advancing contact angle, θ_{adv}. The system tends to achieve the receding contact angle when liquid is removed (for example, at the rear end of a moving droplet), whereas the advancing contact angle is achieved when the liquid is added (for example, at the front end of a moving droplet). When the liquid is neither added nor removed, the system tends to have a static or 'most stable' contact angle, which is given approximately by equations (5)–(10). The difference between θ_{adv} and θ_{rec} is known as the 'contact angle hysteresis' and it reflects a fundamental asymmetry of wetting and dewetting and the irreversibility of the wetting/dewetting cycle. Although for surfaces with a roughness that is carefully controlled on the molecular scale it is possible to achieve contact angle hysteresis as low as $<1^\circ$ (Gupta *et al* 2005), it cannot be eliminated completely, since even the atomically smooth surfaces have a certain roughness and heterogeneity. The contact angle hysteresis is a measure of energy dissipation during the flow of a droplet along a solid surface. A water-repellent surface should have a low contact angle hysteresis to allow water to flow easily along the surface.

It is emphasized that the contact angle provided by equations (5)–(10) is a macroscale parameter, so it is sometimes called 'the apparent contact angle'. The actual angle under which the liquid–vapor interface comes into contact with the solid surface at the micro- and nanoscale can be different. There are several reasons for that. First, water molecules tend to form a thin layer upon the surfaces of many materials. This is because of a long-distance van der Waals adhesion force that creates the so-called disjoining pressure (Derjaguin and Churaev 1974). This pressure is dependent upon the liquid layer thickness and may lead to formation of stable thin films. In this case, the shape of the droplet near the triple line gradually transforms from a spherical surface into a precursor layer, and thus the nanoscale contact angle is much smaller than the apparent contact angle. In addition, adsorbed water monolayers and multilayers are common for many materials. Second, even carefully prepared atomically smooth surfaces exhibit a certain roughness and chemical heterogeneity. At first water tends to cover the hydrophilic spots with high surface energy and low contact angle (Checco *et al* 2003). The tilt angle due to the roughness can also contribute into the apparent contact angle. Third, the very concept of a static contact angle is not well defined. For practical purposes, the contact angle which is formed after a droplet is gently placed upon a surface and stops propagating is considered to be the static contact angle. However, depositing the droplet involves adding liquid while leaving it may involve evaporation, so it is difficult to avoid dynamic effects. Fourth, for small droplet and curved triple lines, the effect of the contact line tension may be significant. Molecules at the surface of a liquid or solid phase have higher energy because they are bonded to fewer molecules than those in the bulk. This leads to the surface tension and surface energy. In a similar manner, molecules at the edge have fewer bonds than those at the surface, which leads to the line tension and the curvature dependence of the surface energy. This effect becomes important when the radius of curvature is comparable with the so-called Tolman length, normally of the order of molecular size (Anisimov 2007). However, the triple line at the nanoscale can be curved so that the line tension effects become important (Pompe *et al* 2000). Thus while the contact angle is a convenient macroscale parameter, wetting is governed by interactions at the micro- and nanoscale, which determine the contact angle hysteresis and other wetting properties (table 1).

3.4. Range of applicability of the Wenzel and Cassie equations

Gao and McCarthy (2007) showed experimentally that the contact angle of a droplet is defined by the triple line and does not depend upon the roughness under the bulk of the droplet. A similar result for chemically heterogeneous surfaces was obtained by Extrand (2003). Gao and McCarthy (2007) concluded that the Wenzel and Cassie–Baxter equations 'should be used with the knowledge of their fault'. The question remained, however, under what circumstances the Wenzel and Cassie–Baxter equations can be safely used and under what circumstances they become irrelevant.

For a liquid front propagating along a rough two-dimensional profile (figures 2(a) and (b)), the derivative of the free surface energy (per liquid front length), W, by the profile

Table 2. Summary of experimental results for uniform and non-uniform rough and chemically heterogeneous surfaces. For non-uniform surfaces, the results shown are for droplets larger than the islands of non-uniformity. Detailed quantitative values of the contact angle in various sets of experiments can be found in the referenced sources (Nosonovsky 2007c).

Experiment	Roughness/ hydrophobicity at the triple line and at the rest of the surface	Roughness at the bulk (under the droplet)	Experimental contact angle (compared with that at the rest of the surface)	Theoretical contact angle, Wenzel/Cassie equations	Theoretical contact angle, generalized Wenzel–Cassie (equations (16) and (17))
Gao and McCarthy (2007)	Hydrophobic	Hydrophilic	Not changed	Decreased	Not changed
	Rough	Smooth	Not changed	Decreased	Not changed
	Smooth	Rough	Not changed	Increased	Not changed
Extrand (2003)	Hydrophilic	Hydrophobic	Not changed	Increased	Not changed
	Hydrophobic	Hydrophilic	Not changed	Decreased	Not changed
Bhushan *et al* (2007)	Rough	Rough	Increased	Increased	Increased
Barbieri *et al* (2007)	Rough	Rough	Increased	Increased	Increased

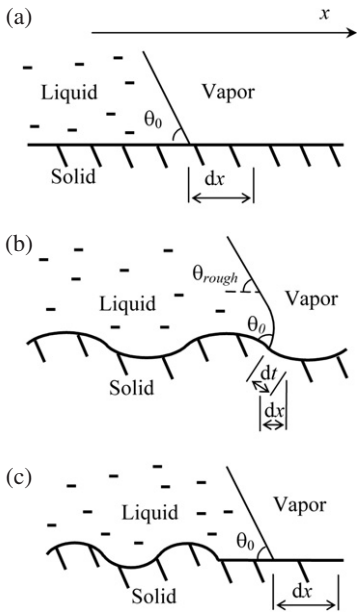

Figure 2. Liquid front in contact with (a) a smooth solid surface and (b) a rough solid surface. Propagation for a distance dt along the curved surface corresponds to the distance dx along the horizontal surface. (c) Surface roughness under the bulk of the droplet does not affect the contact angle.

length, t, yields the surface tension force $\sigma = \mathrm{d}W/\mathrm{d}t = \gamma_{SL} - \gamma_{SV}$. The quantity of practical interest is the component of the tension force that corresponds to the advancing of the liquid front in the horizontal direction for dx. This component is given by $\mathrm{d}W/\mathrm{d}x = (\mathrm{d}W/\mathrm{d}t)(\mathrm{d}t/\mathrm{d}x) = (\gamma_{SL} - \gamma_{SV})\,\mathrm{d}t/\mathrm{d}x$. It is noted that the derivative $R_f = \mathrm{d}t/\mathrm{d}x$ is equal to Wenzel's roughness factor in the case when the roughness factor is constant throughout the surface. Therefore, the Young equation, which relates the contact angle with solid, liquid, and vapor interface tensions, $\gamma_{LV}\cos\theta = \gamma_{SV} - \gamma_{SL}$, is modified as (Nosonovsky 2007c)

$$\gamma_{LV}\cos\theta = R_f(\gamma_{SV} - \gamma_{SL}). \tag{15}$$

The empirical Wenzel equation (equation (6)) is a consequence of equation (15) combined with the Young equation.

Nosonovsky (2007c) showed that for a more complicated case of a non-uniform roughness, given by the profile $z(x)$, the local value of $r(x) = \mathrm{d}t/\mathrm{d}x = (1 + (\mathrm{d}z/\mathrm{d}x)^2)^{1/2}$ matters. In the cases that were studied experimentally by Gao and McCarthy (2007) and Extrand (2003), the roughness was present ($r > 1$) under the bulk of the droplet, but there was no roughness ($r = 0$) at the triple line, and the contact angle was given by equation (6) (figure 2(c)). In the general case of a 3D rough surface $z(x, y)$, the roughness factor can be defined as a function of the coordinates $r(x, y) = (1 + (\mathrm{d}z/\mathrm{d}x)^2 + (\mathrm{d}z/\mathrm{d}y)^2)^{1/2}$.

Whereas equation (6) is valid for uniformly rough surfaces, that is, surfaces with $r = \text{const}$, for non-uniformly rough surfaces the generalized Wenzel equation is formulated to determine the local contact angle (a function of x and y) with a rough surface at the triple line

$$\cos\theta = r(x, y)\cos\theta_0. \tag{16}$$

Equation (6) is consistent with the experimental results of the worker who showed that roughness beneath the droplet does not affect the contact angle, since it predicts that only roughness at the triple line matters. It is also consistent with the results of the researchers who confirmed the Wenzel equation (for the case of the uniform roughness) and of those who reported that only the triple line matters (for non-uniform roughness) (table 2).

The Cassie equation for the composite surface can be generalized in a similar manner, introducing the spatial dependence of the local densities f_1 and f_2 of the solid–liquid interface with the contact angle, as a function of x and y, given by

$$\cos\theta_{\text{composite}} = f_1(x, y)\cos\theta_1 + f_2(x, y)\cos\theta_2 \tag{17}$$

where $f_1 + f_2 = 1$ and θ_1 and θ_2 are contact angles of the two components (Nosonovsky 2007c).

The important question remains, what should be the typical size of roughness/heterogeneity details in order for the generalized Wenzel and Cassie equations (equations (16) and (17)) to be valid? Some researchers have suggested that roughness/heterogeneity details should be comparable with the thickness of the liquid–vapor interface and thus 'the roughness would have to be of molecular dimensions to alter the equilibrium conditions' (Bartell and Shepard 1953), whereas others have claimed that roughness/heterogeneity

details should be small compared with the linear size of the droplet (Johnson and Dettre 1964, Li and Amirfazli 2006, Bhushan *et al* 2007, Barbieri *et al* 2007). The interface in our analysis is an idealized 2D object, which has no thickness. In reality, the triple line zone has two characteristic dimensions: the thickness (of the order of the molecular dimensions) and the length (of the order of the droplet size).

The apparent contact angle, given by equations (16) and (17), may be viewed as the result of averaging of the local contact angle at the triple line by its length, and thus the size of the roughness/heterogeneity details should be small compared with the length (and not the thickness) of the triple line. When the liquid–vapor interface is studied at the length scale of the roughness/heterogeneity details, the local contact angle, θ_0, is given by equations (6)–(10). The liquid–vapor interface at that scale has perturbations caused by the roughness/heterogeneity, and the scale of the perturbations is the same as the scale of the roughness/heterogeneity details. However, when the same interface is studied at a larger scale, the effect of the perturbation vanishes, and the apparent contact angle is given by equations (16) and (17) (figure 2(c)). This apparent contact angle is defined at the scale length, for which the small perturbations of the liquid–vapor interface vanish, and the interface can be treated as a smooth surface. The values of $r(x, y)$, $f_1(x, y)$, and $f_2(x, y)$ in equations (16) and (17) are average values for an area (x, y) with size larger than a typical roughness/heterogeneity detail size. Therefore, the generalized Wenzel and Cassie equations can be used at the scale at which the effect of the interface perturbations vanish, or, in other words, when the size of the solid surface roughness/heterogeneity details is small compared with the size of the liquid–vapor interface, which is of the same order as the size of the droplet.

We used the surface energy approach to find the domain of validity of the Wenzel and Cassie equations (uniformly rough surfaces) and generalized it for a more complicated case of non-uniform surfaces. The generalized equations explain a wide range of existing experimental data, which could not be explained by the original Wenzel and Cassie equations.

4. Calculation of the contact angle for selected surfaces

The contact angle of a liquid with a number of rough surfaces is calculated in this section. The model presented in the preceding sections combines the effect of surface area, the possibility of formation of a composite interface, and the effect of sharp edges. Several selected rough surfaces are considered (shown in figure 3). First, two-dimensional surface profiles are analyzed, followed by more complex three-dimensional surfaces. Based on the analysis, roughness optimization for the contact angle was conducted by Nosonovsky and Bhushan (2005).

4.1. Two-dimensional periodic profiles

4.1.1. Sawtooth periodic profile. Let us consider a surface with a sawtooth profile with a tooth angle (or the absolute value of slope) of α (figure 3). Using equation (6), the roughness factor is calculated as

$$R_f = \frac{A_{SL}}{A_F} = (\cos\alpha)^{-1}. \tag{18}$$

Using equation (6), the contact angle is given as

$$\cos\theta = \frac{\cos\theta_0}{\cos\alpha}. \tag{19}$$

An increase of α above $\alpha_0 = 180^\circ - \theta_0$ will result in a transition from a complete solid–liquid contact to a composite solid–liquid–air interface, and equation (19) cannot be used any further. Substituting the value of slope $\alpha = \alpha_0$ into equation (19), the value of θ, which corresponds to α_0, can be obtained; this gives that the critical value α_0 corresponds to the contact angle $\theta = 180^\circ$. This means that by increasing the tooth angle toward the critical value, a surface with a contact angle approaching 180° can be produced for a given θ_0. However, sharp edges, which may lead to pinning of the triple line, make the sawtooth profile undesirable. In addition to this, the sawtooth profile provides roughness only in the direction perpendicular to the grooves, which may act as open capillaries to reinforce wetting, which is also undesirable (Nosonovsky and Bhushan 2005).

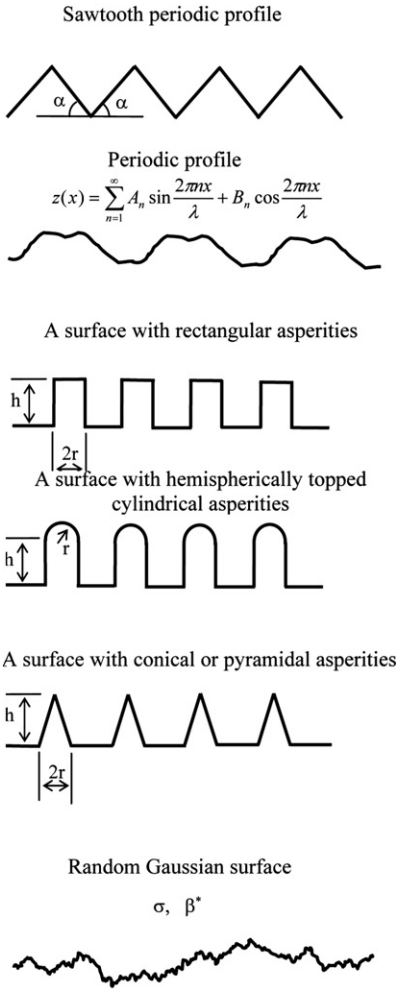

Figure 3. Various rough surfaces (Nosonovsky and Bhushan 2005).

4.1.2. General periodic profile. For a general form of the surface $z(x, y)$, the solid–liquid area of contact is equal to

$$A_{SL} = A_F \iint_{A_F} \sqrt{1 + \left(\frac{\partial z}{\partial x}\right)^2 + \left(\frac{\partial z}{\partial y}\right)^2}\, dx\, dy. \quad (20)$$

A periodic two-dimensional surface profile with the period λ can be presented as a Fourier series

$$z(x) = \sum_{n=1}^{\infty} A_n \sin\frac{2\pi nx}{\lambda} + B_n \cos\frac{2\pi nx}{\lambda}. \quad (21)$$

The derivatives of $z(x)$ are given as

$$\frac{dz}{dx} = \frac{2\pi}{\lambda}\sum_{n=1}^{\infty} A_n n \cos\frac{2\pi nx}{\lambda} - B_n n \sin\frac{2\pi nx}{\lambda}$$
$$\frac{dz}{dy} = 0. \quad (22)$$

Substituting equations (22) and (20) into equation (7) provides us with an expression for the roughness factor of a periodic profile (Nosonovsky and Bhushan 2005)

$$R_f = \frac{1}{\lambda}\int_0^{\lambda} \sqrt{1 + \frac{4\pi^2}{\lambda^2}\left(\sum_{n=1}^{\infty} A_n n \cos\frac{2\pi nx}{\lambda} - B_n n \sin\frac{2\pi nx}{\lambda}\right)^2}\, dx. \quad (23)$$

It is possible to determine whether a composite interface is possible by considering the slope of the profile. In order for a composite interface to form, the absolute value of the slope must exceed the critical angle α_0 at any point

$$\left|\frac{2\pi}{\lambda}\sum_{n=1}^{\infty} A_n n \cos\frac{2\pi nx}{\lambda} - B_n n \sin\frac{2\pi nx}{\lambda}\right| > \tan(\alpha_0) = \tan(-\theta_0). \quad (24)$$

As an example, let us consider a sinusoidal profile

$$z(x) = A_1 \sin\frac{2\pi x}{\lambda}. \quad (25)$$

By substituting equation (25) into (23) and integrating, a closed-form solution can be obtained (Nosonovsky and Bhushan 2005):

$$R_f = \frac{1}{\lambda}\int_0^{\lambda} \sqrt{1 + (2\pi A_1/\lambda)^2 \cos^2(2\pi x/\lambda)}\, dx$$
$$= \frac{1}{2\pi}\int_0^{2\pi} \sqrt{1 + (2\pi A_1/\lambda)^2 \cos^2 x}\, dx$$
$$= \frac{2}{\pi}\sqrt{1 + (2\pi A_1/\lambda)^2}\int_0^{\pi/2} \sqrt{1 - \frac{(2\pi A_1/\lambda)^2}{1 + (2\pi A_1/\lambda)^2}\sin^2 x}\, dx$$
$$= \frac{2}{\pi}\sqrt{1 + (2\pi A_1/\lambda)^2}\, E\left(\frac{(2\pi A_1/\lambda)}{\sqrt{1 + (2\pi A_1/\lambda)^2}}\right) \quad (26)$$

where $E(x)$ is the so-called elliptical integral of the second kind, the values of which are tabulated in handbooks

$$E(k) = \int_0^{\pi/2} \sqrt{1 - k^2 \sin^2 x}\, dx. \quad (27)$$

The maximum absolute value of the slope of the sinusoidal profile (equation (25)) is achieved at $x = 0$ and is equal to $2\pi A_1/\lambda$. With an increase of A_1/λ the slope increases, and a composite interface may be formed (figure 4(a)). For a composite interface to form, the slope at some points should exceed the critical value α_0. By using equation (24) and setting $x = 0$, the condition for existence of the composite interface is found as

$$\frac{2\pi A_1}{\lambda} > \tan(-\theta_0). \quad (28)$$

The contact angle can be calculated by substituting R_f from equation (26) into (6). The dependence of the contact angle on amplitude for the sinusoidal profile is presented in figure 4(a). It is observed, that lower values of θ correspond to lower values of θ_0 at the transition to the composite interface, unlike in the case of the sawtooth surface which has critical values corresponding to $\theta_0 = 180°$. For $\theta_0 = 100°$ the critical value of $R_f = 5.67$ ($\theta = 131°$), for $\theta_0 = 120°$ the critical value of $R_f = 1.73$ ($\theta = 140°$), and for $\theta_0 = 150°$ the critical value of $R_f = 0.58$ ($\theta = 159°$). Further increase of A_1/λ may lead to a corresponding increase of R_f and θ (Zhou and De Hosson 1995). However, as will be discussed below, the composite interface can be destabilized. Therefore, the sinusoidal interface is not recommended for producing superhydrophobic surfaces. In addition to this, the sinusoidal profile provides roughness only in the direction perpendicular to the grooves, which may act as open capillaries to reinforce wetting, which is also undesirable (Nosonovsky and Bhushan 2005).

4.2. Three-dimensional surfaces

The analysis of profiles provides critical values of the roughness parameters in the case when the contact line is parallel to the grooves. Three-dimensional surfaces, which constitute a more general case, with various typical shapes of asperities are considered in this subsection.

4.2.1. Array of asperities of identical shape and size. Let us consider a rough surface with rectangular asperities, which have a square foundation with side $2r$ and height h (figure 3). For each asperity, the area of surface is given by

$$A_{asp} = 8rh + 4r^2 \quad (29)$$

whereas the flat projection area is $4r^2$. Assuming that asperities are randomly distributed throughout the surface with a density of η asperities per unit area, the total contact surface area is given by

$$A_{SL} = A_F + A_F\eta(8rh + 4r^2) - A_F 4\eta r^2 = A_F(1 + 8\eta r^2). \quad (30)$$

The roughness factor is found using equations (7) and (30)

$$R_f = 1 + 8\eta rh = 1 + 2p^2 h/r \quad (31)$$

where p is a packing parameter which characterizes the packing of the asperities; for asperities with a square foundation, $p = 2r\sqrt{\eta}$. The packing parameter is equal to the fraction of the surface area which is covered by asperities.

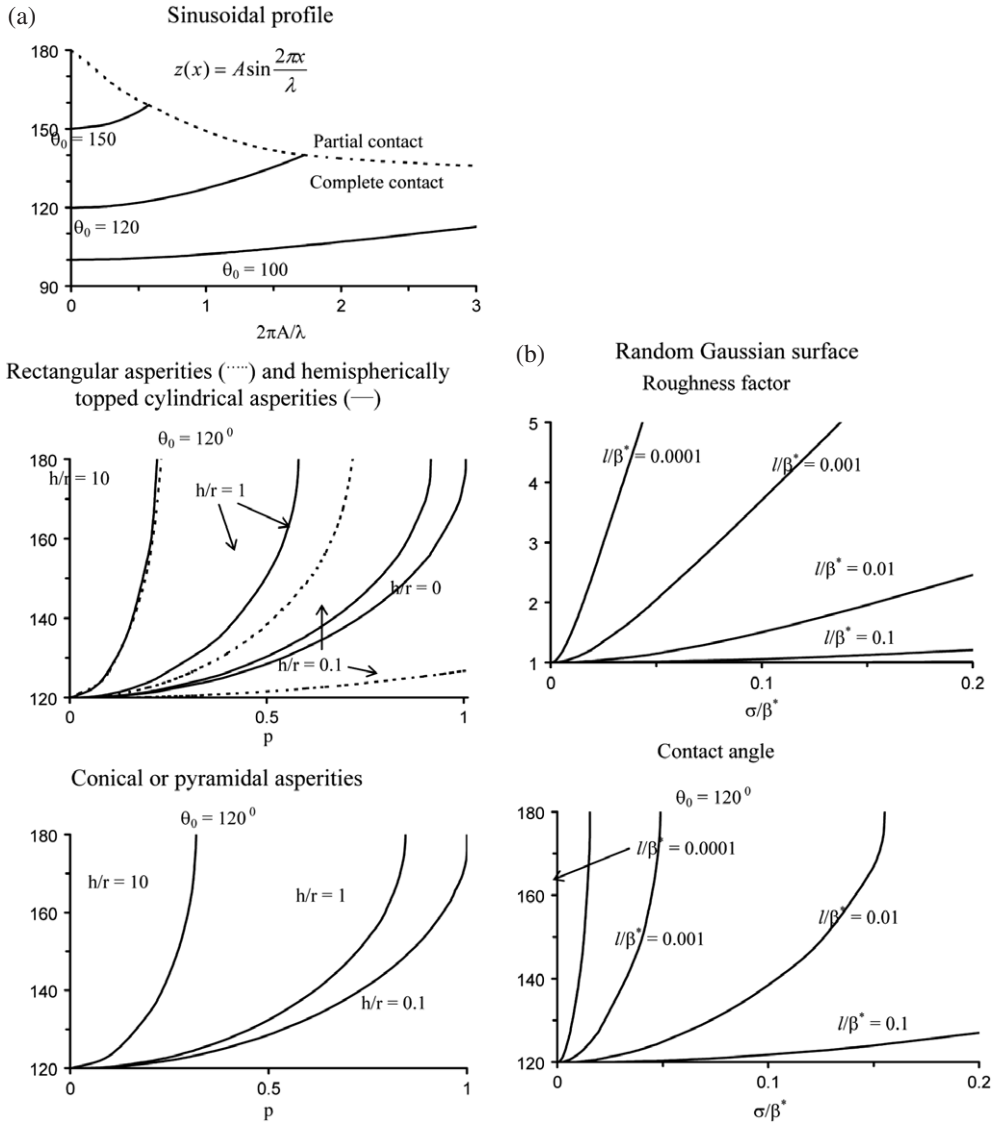

Figure 4. (a) Contact angle for a rough surface (θ) as a function of surface parameters for a surface with a sinusoidal profile, rectangular (dotted line)/hemispherically topped cylindrical (solid line) and conical/pyramidal asperities. (b) Dependence of the roughness factor (R_f) and contact angle for rough surface (θ) on roughness parameters for a Gaussian surface (Nosonovsky and Bhushan 2005).

In a similar manner R_f can be calculated for asperities with cylindrical foundation of height h and hemispherical top of radius r (figure 3). For each asperity, the area of surface is given by

$$A_{asp} = 2\pi r^2(1 + h/r) \tag{32}$$

whereas the flat projection area is given by πr^2. Assuming that asperities are randomly distributed throughout the surface with a density of η asperities per unit area, the total contact surface area is given by

$$\begin{aligned} A_{SL} &= A_F + A_F\eta 2\pi r^2(1 + h/r) - A_F\eta\pi r^2 \\ &= A_F[1 + \eta\pi r^2(1 + 2h/r)]. \end{aligned} \tag{33}$$

The roughness factor is found using equations (7) and (33):

$$R_f = 1 + \eta\pi r^2(1 + 2h/r) = 1 + p^2(1 + 2h/r) \tag{34}$$

where the packing parameter for asperities with a circular foundation is $p = r\sqrt{\pi\eta}$ (Nosonovsky and Bhushan 2005).

For conical asperities of height h, radius r, and side length $L = \sqrt{h^2 + r^2}$, we can obtain in a similar manner

$$A_{asp} = \pi r^2(1 + L/r) \tag{35}$$

$$\begin{aligned} A_{SL} &= A_F + A_F\eta\pi r^2(1 + L/r) - A_F\eta\pi r^2 = A_F(1 + \eta\pi rL) \\ &= A_F\left(1 + \eta\pi r^2\sqrt{1 + (h/r)^2}\right) \end{aligned} \tag{36}$$

and

$$\begin{aligned} R_f &= 1 + \eta\pi rL = 1 + \eta\pi r^2\sqrt{1 + (h/r)^2} \\ &= 1 + p^2\sqrt{1 + (h/r)^2} \end{aligned} \tag{37}$$

where the packing parameter, for asperities with a circular foundation, is $p = r\sqrt{\pi\eta}$ (Nosonovsky and Bhushan 2005).

For pyramidal asperities with square foundation of width $2a$ and height h, the corresponding quantities are given as

$$A_{asp} = 4r^2\left(1 + \sqrt{1 + (h/r)^2}\right) \tag{38}$$

$$A_{SL} = A_F + 4A_F\eta r^2\left(1+\sqrt{1+(h/r)^2}\right) - 4A_F\eta r^2$$
$$= A_F\left(1+4\eta r^2\sqrt{1+(h/r)^2}\right) \quad (39)$$

and

$$R_f = 1+4\eta r^2\sqrt{1+(h/r)^2} = 1+p^2\sqrt{1+(h/r)^2} \quad (40)$$

where the packing parameter, for asperities with a square foundation, is $p = 2r\sqrt{\eta}$ (Nosonovsky and Bhushan 2005).

The dependence of the contact angle on the normalized radius of the asperities (taken as p) for $\theta_0 = 120°$ and for different ratios of h/r is presented in figure 4(a), on the basis of equations (6), (31), (34), (38), and (40), for rectangular, hemispherically topped, conical and pyramidal asperities. It is observed that, with an increase in p, the value of the contact angle increases and reaches 180°. For higher aspect ratios, the increase in θ is faster.

In order to determine the critical values of roughness parameters, which correspond to the transition to the composite interface, it should be analyzed whether the local slope can exceed the critical value α_0 and whether the composite interface is likely to remain stable. It is difficult to conduct such an analysis, due to its complexity; however, an estimate can be made using the fact that with increasing average absolute value of the slope of the surface both the local slope increases and the destabilization of the composite interface becomes less likely, since the surface is less smooth. Based on this, we assume here that, in a similar manner as for the two-dimensional profiles, the absolute value of the surface slope is responsible for transition to the composite liquid–solid–air interface, and consider an average absolute value of the slope. For rectangular, hemispherically topped, conical, and pyramidal asperities, the mean absolute value of the slope, m, is equal to the density of the asperities and the flat projection area times the average absolute value of the slope (equal to twice the aspect ratio):

$$m = \eta\pi r^2(h/r) = \eta\pi hr. \quad (41)$$

The critical value can be found, using a similar approach to the derivation of equations (24):

$$m_0 = \eta\pi hr = \tan(180° - \theta_0) = \tan(-\theta_0). \quad (42)$$

Based on equations (31), (34), (37), (40), and (42), it may be shown that, for the selected value of $\theta_0 = 120°$, for rectangular, hemispherically topped, conical, and pyramidal asperities, the contact angle may approach 180° before the critical value of roughness is reached for the values of h/r shown in figure 4 (Nosonovsky and Bhushan 2005).

The equations developed here are used to calculate contact angle for a lotus leaf and compare it with measured data. The lotus leaf has almost hemispherically topped asperities (papillae) which are covered with wax (Neinhuis and Barthlott 1997, Wagner *et al* 2003). The static contact angle for a water droplet against a paraffin wax surface was reported by Craig *et al* (1960) as 104° and by Kamusewitz *et al* (1999) as 103°. Based on the data reported by Wagner *et al* (2003), the number of asperities (papillae) can be estimated for the lotus leaf as 3400 mm^{-2} ($\eta = 0.0034\ \mu m^{-2}$), the average radius of hemispherically topped asperities $r = 10\ \mu m$, and the aspect ratio $h/r \sim 1$. Based on equation (6), these parameter values correspond to the roughness factor $R_f \sim 4$ and the contact angle $\theta = 165°$ (using $\theta_0 = 104°$ for wax). During the measurements conducted in our lab, the value of the static contact angle for deionized water on a lotus leaf was found to be 156° ± 2° (Burton and Bhushan 2006). Neinhuis and Barthlott (1997) reported a contact angle value of 162° for a water droplet on a lotus leaf.

4.2.2. Random rough surface. A nominally flat random rough surface can be considered as a superposition of a flat plane and a two-dimensional random process, which is characterized by a height distribution and an autocorrelation function. Many engineered and natural rough surfaces can be characterized by a Gaussian height distribution and exponential autocorrelation function (Bhushan 1999, 2002). In this case, a rough surface is described by only two parameters: the standard deviation of asperity heights, σ, and correlation length, β^*. The correlation length β^*, is a spatial parameter and it can be viewed as a measure of randomness. The correlation length, β^*, is responsible for the horizontal scale of the surface, whereas σ is responsible for the vertical scale of the surface. Measured roughness is dependent on the short- and long-wavelength limit of measurement (Bhushan 1999, 2002).

The absolute value of slope of a Gaussian surface also has a Gaussian distribution with the mean

$$m = \frac{\sigma}{l}\sqrt{\frac{1-[\exp(-\beta^*/l)]^2}{\pi}} \quad (43)$$

where l is the sampling interval or short-wavelength limit, which is a distance between data points during a measurement (Whitehouse and Archard 1970). For a surface, the sampling interval is given by a low-wavelength limit of the Gaussian roughness, and is comparable with the atomic dimensions (Nosonovsky and Bhushan 2005).

An element of the area of a surface with slopes of $\partial z/\partial x$ and $\partial z/\partial y$ in the x- and y-directions is given by

$$dA = \sqrt{1+(\partial z/\partial x)^2+(\partial z/\partial y)^2}\,dx\,dy. \quad (44)$$

The distribution of $\sqrt{1+(\partial z/\partial x)^2+(\partial z/\partial y)^2}$ is not Gaussian in general, but in most applications the slope is small and the mean value of slope m can be taken to calculate the mean value of $\sqrt{1+(\partial z/\partial x)^2+(\partial z/\partial y)^2}$. It can also be assumed that slopes in the x- and y-directions are the same. Using equation (21) and m, and integrating, the roughness factor can be calculated (Nosonovsky and Bhushan 2005) as

$$R_f = \iint_{A_f}\sqrt{1+(\partial z/\partial x)^2+(\partial z/\partial y)^2}\,dx\,dy$$
$$= 1+\sqrt{1+2m^2} = \sqrt{1+2\frac{\sigma^2}{l^2}\frac{1-\exp(-l/\beta^*)^2}{\pi}}. \quad (45)$$

For small l/β^*

$$R_f \approx \sqrt{1+2\left(\frac{\sigma}{\beta^*}\right)^2\frac{2}{\pi(l/\beta^*)}}. \quad (46)$$

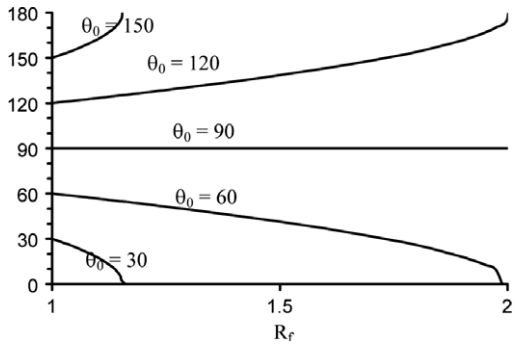

Figure 5. The contact angle for a rough surface (θ) as a function of the roughness factor (R_f) for various contact angles for smooth surfaces (θ_0) (Nosonovsky and Bhushan 2005).

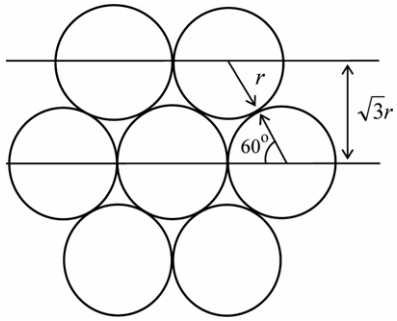

Figure 6. Hexagonal (honeycomb) pattern of packing of circular asperities for the highest packing density (Nosonovsky and Bhushan 2005).

Furthermore, for small values of $\sigma^2/(l\beta^*)$

$$R_f \approx 1 + \frac{2}{\pi}\left(\frac{\sigma}{\beta^*}\right)^2\left(\frac{\beta^*}{l}\right). \tag{47}$$

In order to estimate the critical value of the roughness parameters, we assume, as in the previous subsection, that the average absolute value of the surface slope is responsible for transition to the composite solid–liquid–air interface. The absolute value of the slope is given by equation (43), so, in a similar manner as in derivation of equation (42), the critical values of the Gaussian surface roughness parameters is

$$m_0 = \left(\frac{\sigma}{l}\sqrt{\frac{1-[\exp(-\beta^*/l)]^2}{\pi}}\right)_0 = \tan(-\theta_0). \tag{48}$$

The dependence of the roughness factor on σ/β^* is presented in figure 6(b) based on equation (45). Using the roughness factor, the dependence of the contact angle on σ/β^* is presented in figure 4(b). It is observed, that both the roughness factor and the contact angle increase with increasing σ/β^*. Based on equation (48), it may be shown that, for the selected value of $\theta_0 = 120°$, the contact angle may approach 180° prior to the critical values of the roughness parameters being reached for the values of σ/β^* and l/β^* shown. It is noted that, for most natural and engineering Gaussian surfaces, the ratio $\sigma/\beta^* \ll 0.1$ and the average value of slope is small ($m \ll 1$). Therefore, although the roughness is below the critical value it is difficult to achieve high contact angles with Gaussian random surfaces with a realistic value of σ/β^* (Nosonovsky and Bhushan 2005). The dependence based on the Wenzel equation is shown for comparison in figure 5.

4.3. Surface optimization for maximum contact angle

Among the several types of surfaces considered in the preceding subsections, the highest contact angles are achieved with the sawtooth profile and rectangular/hemispherically topped/conical/pyramidal asperities. As stated earlier, the sawtooth profile is undesirable due to its sharp edges, which may pin the triple line, and because the grooves may reinforce wetting. Therefore, the rectangular, hemispherically topped, conical, and pyramidal asperities should be considered as the most appropriate for producing the highest contact angles. In order to prevent contact angle hysteresis, it is desirable to avoid asperities with sharp edges, which may cause pinning of the triple line. Therefore, hemispherically topped asperities are the most appropriate. A case also will be made later for pyramidal asperities.

Two-tiered roughness, involving two wavelengths, has been considered by some authors (e.g. Herminghaus 2000) to decrease wetting. However, it is more likely to involve sharp edges, which are undesirable, and lead to an unstable composite solid–liquid–air interface.

Based on equations (24), (27), and (40), and on the results shown in figure 4, the maximum contact angle can be achieved by increasing the aspect ratio h/r and the packing parameter p. The maximum aspect ratio may be achieved by increasing asperity height. The maximum packing parameter may be achieved by packing the asperities as tight as possible. The square of the packing parameter p^2 is equal to the ratio of the foundation area of the asperities to the total surface area; therefore, higher values of p correspond to a higher packing density. For asperities with a circular foundation, the square pattern of asperity distribution results in packing of $1/(2r)$ rows per unit area with $1/(2r)$ asperities per unit length in the row. A higher density of asperity packing can be achieved by a hexagonal (honeycomb) distribution of asperities (figure 6). This distribution pattern results in packing of $1/(\sqrt{3}r)$ rows of asperities per unit length with $1/(2r)$ asperities per unit length in the row, or $\eta = 1/(2\sqrt{3}r^2)$, which yields

$$p = r\sqrt{\pi\eta} = \sqrt{\frac{\pi}{2\sqrt{3}}} \approx 0.952. \tag{49}$$

Therefore, the recommendation for surface optimization is to take hexagonally packed hemispherically topped asperities with a high aspect ratio (needle-like). It is noted that certain leaves tend to have a distribution of the papillae close to the hexagonal (honeycomb) (Nosonovsky and Bhushan 2005).

An alternative shape, which provides a packing density $p = 1$, is given by pyramidal asperities with a square foundation. In order to avoid pinning due to sharp edges, the tops may be rounded with hemispheres. Rectangular asperities do not provide space for liquid to penetrate, therefore in the case of asperities with a square foundation, a pyramidal shape

should be used. It should be noted that valleys with rounded edges have the same effect on contact angle as asperities do (Nosonovsky and Bhushan 2005).

The foundation radius of individual asperities, r (for circular foundations) or the foundation side length $2r$ (for square foundations) should be small compared to typical droplets. The upper limit of droplet size may be estimated based on the requirement that the gravity effect is small compared to the surface tension (a bigger droplet is likely to be divided into several small droplets). The gravitational energy of the droplet is given by its density ρ multiplied by the volume, gravitational constant $g = 9.81\ \mathrm{m\ s^{-2}}$, and radius

$$W_g = \tfrac{4}{3}\pi r^3 \rho g r \tag{50}$$

whereas the energy due to the surface tension can be estimated by the droplet surface area multiplied by the surface tension

$$W_g = 4\pi r^2 \gamma_{LA}. \tag{51}$$

Based on $W_g \ll W_s$, we find that the maximum droplet radius is smaller than the capillary length

$$r_{max} \ll \sqrt{\frac{3\gamma_{LA}}{\rho g}}. \tag{52}$$

Typical quantities for water, $\rho = 1000\ \mathrm{kg\ m^{-3}}$ and $\gamma_{LA} = 72\ \mathrm{mJ\ m^{-2}}$ result in $r_{max} \ll 4.7$ mm. Although the small droplets will tend to unite into bigger ones, the minimum droplet radius is limited only by molecular scale, so it is desirable to have r as small as possible.

To summarize, the highest possible contact angle and lowest contact angle hysteresis, which is desirable in applications, may be achieved by using hemispherically topped asperities with hexagonal packing pattern or pyramidal asperities with a rounded top. These recommendations can be used for producing superhydrophobic surfaces (Nosonovsky and Bhushan 2005).

For wetting liquids, roughness results in a decreased contact angle, in accordance with equation (6). Therefore, in order to create a superhydrophobic surface using the effect of roughness, a hydrophobic film is required. Hydrophobic coating is a well-known method of increasing the water-repellency of a material (Satas 1991).

5. Contact angle hysteresis

A sharp edge can pin the line of contact of the solid, liquid, and air (also known as the 'triple line') at a position far from stable equilibrium, i.e. at contact angles different from θ_0 (Eustathopoulos *et al* 1999). This effect is illustrated in the bottom sketch of figure 7, which shows a droplet propagating along a solid surface with grooves. At the edge point, the contact angle is not defined and can have any value between the values corresponding to the contact with the horizontal and inclined surfaces. For a droplet moving from left to right, the triple line will be pinned at the edge point until it is able to proceed to the inclined plane. As is observed from figure 7, the change of the surface slope (α) at the edge is the reason for

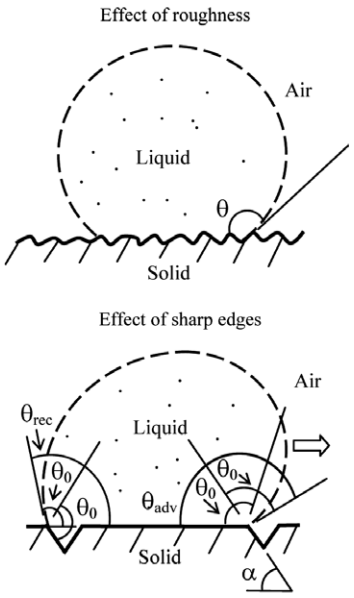

Figure 7. Droplet of liquid in contact with a solid surface—smooth surface, contact angle θ_0; rough surface, contact angle θ—and a surface with sharp edges. For a droplet moving from left to right on a sharp edge (shown by the arrow), the contact angle at a sharp edge may be any value between the contact angle with the horizontal plane and with the inclined plane. This effect results in a difference between advancing ($\theta_{adv} = \theta_0 + \alpha$) and receding ($\theta_{rec} = \theta_0 - \alpha$) contact angles (Nosonovsky and Bhushan 2005).

the pinning. Because of the pinning, the value of the contact angle at the front of the droplet (dynamic maximum advancing contact angle or $\theta_{adv} = \theta_0 + \alpha$) is greater than θ_0, whereas the value of the contact angle at the back of the droplet (dynamic minimum receding contact angle or $\theta_{rec} = \theta_0 - \alpha$) is smaller than θ_0. This phenomenon is known as contact angle hysteresis (Johnson and Dettre 1964, Israelachvili 1992, Eustathopoulos *et al* 1999). A hysteresis domain of the dynamic contact angle is thus defined by the difference $\theta_{adv} - \theta_{rec}$. The liquid can travel easily along the surface if the contact angle hysteresis is small. It is noted that the static contact angle lies within the hysteresis domain, therefore increasing the static contact angle up to the values of a superhydrophobic surface (approaching 180°) will also result in a reduction of contact angle hysteresis. In a similar manner, contact angle hysteresis also can exist even if the surface slope changes smoothly, without sharp edges.

For a micropatterned surface built of flat-top columns ($R_f = 1$), contact angle hysteresis involves a term inherent to the nominally smooth surface and a term dependent upon the surface roughness, H_r. Using the same approach as in the derivation of equation (12) for the advancing and receding contact angles, one finds

$$\cos\theta_{adv} - \cos\theta_{rec} = f_{SL}(\cos\theta_{adv0} - \cos\theta_{rec0}) + H_r \tag{53}$$

where θ_{adv0} and θ_{rec0} are the advancing and receding contact angles for the smooth surface (Bhushan *et al* 2007, Nosonovsky 2007b). The first term in the right-hand part of the equation (53), which corresponds to the inherent contact angle hysteresis of a smooth surface, is proportional to the fraction of the solid–liquid contact area, f_{SL}. The second term, H_r, may

be assumed to be proportional to the length density of the pillar edges, or, in other words, to the length density of the triple line (Bhushan *et al* 2007). Thus equation (53) involves both the term proportional to the solid–liquid interface area and to the triple line length.

6. Stability of the composite interface

As was pointed out in the preceding sections, although a homogeneous interface may be possible geometrically, it may be unstable, so that the stability of a homogeneous interface should be analyzed. Mathematically, this means that in addition to satisfying the equilibrium condition for the net energy

$$\mathrm{d}E = 0 \tag{54}$$

the stable configuration should satisfy the minimum net energy condition

$$\mathrm{d}^2E > 0. \tag{55}$$

The interface may be destabilized due to small perturbations caused by various external influences and effects, for example by the capillary or gravitational waves. Furthermore, the configuration may have many stable equilibrium conditions (metastability) and may be transformed from one stable position to another due to the external effects, with a certain probability of finding the system at a given state. These phenomena are considered in the present section.

6.1. Destabilization due to capillary and gravitational waves

A wave may form at the liquid–air interface due to gravitational or capillary forces

$$z = A\cos(kx - \omega t) \tag{56}$$

where z is vertical displacement, k and ω are the wavenumber and frequency, which are related to each other as

$$\omega^2 = gk + \frac{\gamma_{\mathrm{LA}}}{\rho}k^3 \tag{57}$$

where g is the gravity constant, ρ is the liquid density and γ_{LA} is the liquid–air interface energy (Landau and Lifshitz 1959). For most micro-/nanoscale applications, the effect of gravity is small and the frequency is given by

$$\omega = \sqrt{\frac{\gamma_{\mathrm{LA}}k^3}{\rho}}. \tag{58}$$

The capillary waves may lead to composite interface destabilization, as will be shown below (Nosonovsky and Bhushan 2006a).

It is assumed that the interface energy γ_{LA} is a constant for given materials and that it is size independent. Generally speaking, this is not true for a very small thickness of liquid comparable with the range of intermolecular forces. However, in the present work we are assuming that the relevant size of the surface roughness, as well as the thickness of the liquid layer, is greater than the range of the intermolecular forces and therefore that γ_{LA} is constant.

Consider a sawtooth profile, figure 8(a), with tooth height $a\tan\alpha/2$ and distance between the teeth d. The teeth represent the asperities of a rough surface. It is assumed that the model of the sawtooth profile can capture important features of more complicated rough surfaces. The horizontal liquid–air interface is located at a distance z from the valley and has small waves of amplitude A and wavenumber k. The total change of the energy of the system from the energy of the homogeneous solid–liquid interface is given by the sum of surface changes throughout the inclined and horizontal portions of the surface and corresponding liquid–air parts, plus the wave energy. The changes in surface energy at inclined and horizontal portions of the surfaces and at corresponding liquid–air parts are given by the lengths of the corresponding surfaces times the corresponding interface energies. The length of the inclined portion of the interface is $z/\sin\alpha$ and the length of the corresponding section of the wavy surface is $(z/\tan\alpha)(kL_0/2\pi)$, where L_0 is the length of the liquid–air interface per wave period, given by the integral

$$\begin{aligned} L_0 &= \int_0^{2\pi/k}\sqrt{1+(Ak)^2\sin^2(xk)}\,\mathrm{d}x \\ &= 4\sqrt{1+(Ak)^2}\,E\left(\frac{Ak}{\sqrt{1+(Ak)^2}}\right) \end{aligned} \tag{59}$$

where $E(x)$ is an elliptical integral of the second kind (Nosonovsky and Bhushan 2006a). The length of the horizontal portion of the interface is d, and the length of the corresponding section of the wavy surface is $dkL_0/(2\pi)$. The energy change is given by

$$\begin{aligned} U(z) &= -\frac{2z}{\sin\alpha}(\gamma_{\mathrm{SL}}-\gamma_{\mathrm{SA}}) + \frac{2z}{\tan\alpha}\frac{kL_0}{2\pi}\gamma_{\mathrm{LA}} \\ &\quad - d\left[(\gamma_{\mathrm{SL}}-\gamma_{\mathrm{SA}}) - \gamma_{\mathrm{LA}}\frac{kL_0}{2\pi}\right]H(z) + E_0 \\ &= \frac{2z\gamma_{\mathrm{LA}}}{\sin\alpha}\left(\cos\theta_0 + \cos\alpha\frac{kL_0}{2\pi}\right) \\ &\quad + d\gamma_{\mathrm{LA}}\left[\cos\theta_0 + \frac{kL_0}{2\pi}\right]H(z) + E_0 \end{aligned} \tag{60}$$

where E_0 is the energy of the waves, γ_{SL} and γ_{SA} are interface energies for the solid–liquid and solid–air interfaces, correspondingly, and $H(z)$ is the step function, such that $H(z) = 0$ for $z \leqslant 0$ and $H(z) = 1$ for $z > 0$. It is assumed in equation (60) that $z > A$ and the Young equation is used.

In the limiting case of a flat liquid–air interface ($A = 0$), the surface energy is given by Nosonovsky and Bhushan (2006a)

$$\begin{aligned} U(z) &= -\frac{2z}{\sin\alpha}(\gamma_{\mathrm{SL}}-\gamma_{\mathrm{SA}}) + \frac{2z}{\tan\alpha}\gamma_{\mathrm{LA}} \\ &\quad - d[(\gamma_{\mathrm{SL}}-\gamma_{\mathrm{SA}}) - \gamma_{\mathrm{LA}}]H(z) \\ &= \frac{2z\gamma_{\mathrm{LA}}}{\sin\alpha}(\cos\theta_0+\cos\alpha) \\ &\quad + d\gamma_{\mathrm{LA}}(\cos\theta_0+1)H(z) \qquad A < z. \end{aligned} \tag{61}$$

For $z > 0$, the energy may increase or decrease with increasing z, depending on the sign of $(\cos\theta_0+\cos\alpha)$, since both γ_{LA} and $\sin\alpha$ are positive. In particular, if $180^\circ - \alpha > \theta_0$, the energy increases with z, otherwise it decreases. The stable position corresponds to the minimum value of the energy, which is

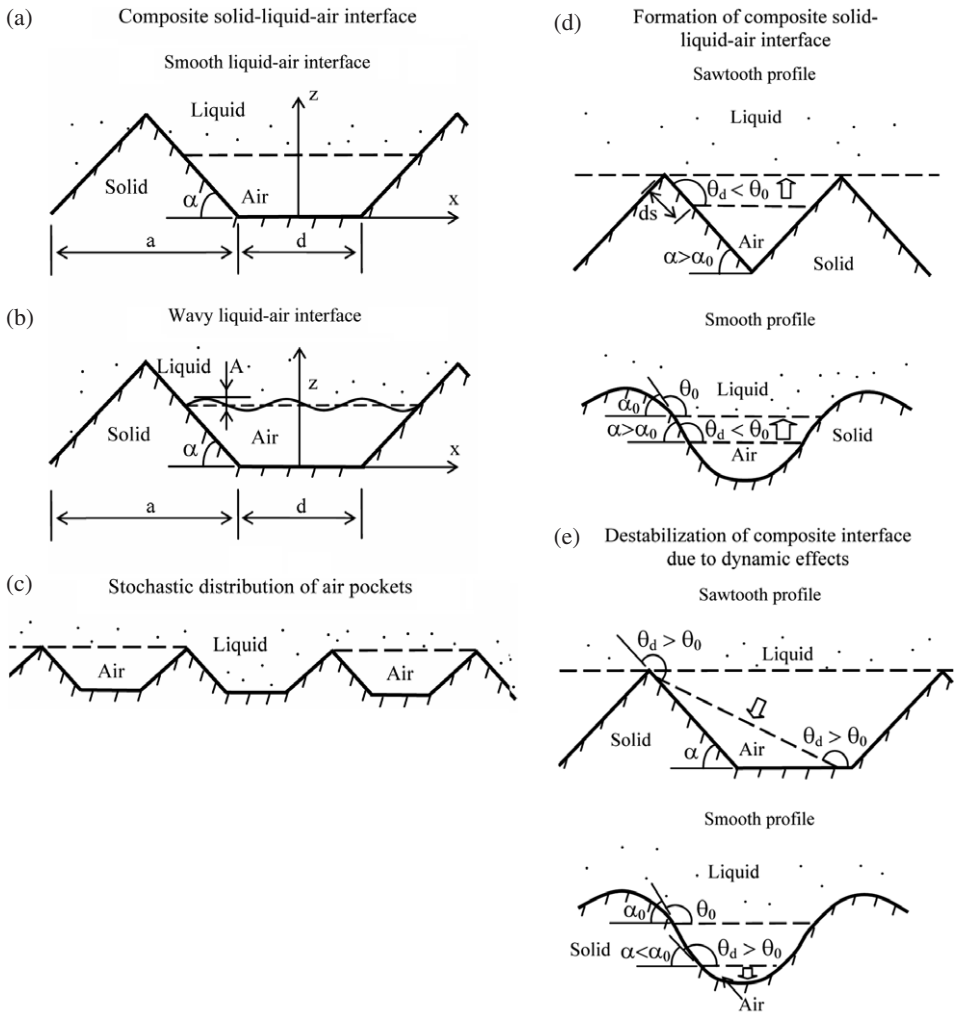

Figure 8. Sawtooth profile: (a) with smooth liquid–air interface, (b) with wavy liquid–air interface, and (c) with stochastic distribution of air pockets (Nosonovsky and Bhushan 2006a). (d) Formation of a composite solid–liquid–air interface for sawtooth and smooth profiles and (e) destabilization of the composite interface for the sawtooth and smooth profiles due to dynamic effects. The dynamic contact angle $\theta_d > \theta_0$ corresponds to an advancing liquid–air interface, whereas $\theta_d < \theta_0$ corresponds to a receding interface (Nosonovsky and Bhushan 2005).

$z = a/(2\tan\alpha)$ (liquid staying at the tops of the asperities) for $180^\circ - \alpha < \theta_0$ and $z = 0$ for $180^\circ - \alpha > \theta_0$ (homogeneous solid–liquid interface).

For a wavy liquid air interface, based on equation (60), the energy may increase with increasing z, if $\cos\theta_0 + \cos\alpha k L_0/(2\pi) > 0$, for $z > A$. However, for $z < A$, the waves touch the horizontal part of the interface and only the fraction $(\pi - \arccos(z/A))/\pi$ of the interface is liquid–air. In this case the energy change is given by

$$U(z) = \frac{z\gamma_{LA}}{\sin\alpha}\left[\cos\theta_0 + \frac{\pi - \arccos(z/A)}{\pi}\left(\frac{kL_{LA}}{2\pi}\right)\cos\alpha\right] + d\gamma_{LA}\left(\cos\theta_0 + \frac{kL_{LA}}{2\pi}\right)\frac{\pi - \arccos(z/A)}{\pi}H(z) + E_0 \qquad A > z \tag{62}$$

where L_{LA} is the length of the liquid–air part of the interface (the wave not touching the solid horizontal part of the interface) given by Nosonovsky and Bhushan (2006a)

$$L_{LA} = \int_{-ar\cos(z/A)/k}^{ar\cos(z/A)/k} \sqrt{1 + (Ak)^2\sin^2(xk)}\,dx. \tag{63}$$

The energy change U as a function of the position of the liquid–air interface z is presented in figure 9 for the smooth interface (equation (61)) and for the wavy liquid–air interface (equations (60) and (62)). It is noted that in the case when the waves are introduced $U(z)$ has a local minimum at $z = 0$, which corresponds to a homogeneous solid–liquid interface, and, in the case of $\cos\theta_0 + \cos\alpha k L_0/(2\pi) < 0$, it has another minimum at $z = a/(2\tan\alpha)$, which corresponds to the composite solid–liquid–air interface (liquid staying at the top of the asperities). The interface position z is normalized in such a manner that the first equilibrium position ($z = 0$) corresponds to zero and the second $z = a/(2\tan\alpha)$ corresponds to unity in figure 9. In this case, the system has two equilibria and may be, with a certain probability, in either one or another position. The interface consists

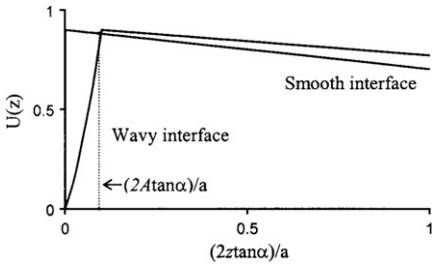

Figure 9. Energy change as a function of interface position for smooth and wavy liquid–air interfaces, $d\gamma_{LA}(\cos\theta_0 + 1) = 0.9$, $\gamma_{LA}(\cos\theta_0 + \cos\alpha)/\sin\alpha = -0.2$, $\gamma_{LA}(\cos\theta_0 + (kL_0/2\pi)\cos\alpha)/\sin\alpha = -0.15$, $E_0 = 0.015$, $A = 0.1$ (Nosonovsky and Bhushan 2006a).

of many asperities and valleys—some of the valleys have a homogeneous interface whereas others have a composite interface (figure 8(b)). It is assumed that the probability p for the interface to be composite depends on the geometrical parameters of the interface and the values of the energy which correspond to the metastable states (Nosonovsky and Bhushan 2006a).

6.2. Stochastic model

In this section, the mechanism of destabilization of the composite interface due to liquid–air interface waves will be considered, and a statistical model for interface destabilization will be discussed (Nosonovsky and Bhushan 2006a). It has been shown in the previous section that the interface may have two stable states. The first stable state corresponds to a homogeneous interface with energy level

$$U(0) = 0. \tag{64}$$

The second metastable state corresponds to a composite interface ($z = a/2\tan\alpha$) with energy level obtained from equation (60)

$$U(a/2\tan\alpha) = \frac{a\gamma_{LA}}{\tan\alpha\sin\alpha}\left(\cos\theta_0 + \cos\alpha\frac{kL_0}{2\pi}\right) + d\gamma_{LA}\left(\cos\theta_0 + \frac{kL_0}{2\pi}\right) + E_0. \tag{65}$$

A certain probability p may be associated with each of the two stable states of energy. Assuming that the waves with energy E_0 have a similar effect on the system, as the thermal fluctuation of an ideal gas with the energy kT, the Maxwell–Boltzmann statistical distribution may be applied (Eyring 1964). Based on the Maxwell–Boltzmann distribution, the probability is exponentially dependent upon the energy level:

$$p = B\exp\left(-\frac{U}{E_0}\right) \tag{66}$$

where B is a normalization constant (Nosonovsky and Bhushan 2006a). Substituting equation (65) into (66) yields the probability of the composite interface

$$p(\phi) = C\exp(-\phi/\phi_0) \tag{67}$$

where

$$\phi = d/a \tag{68}$$

$$\phi_0 = \frac{E_0}{a\gamma_{LA}\left(\cos\theta_0 + \frac{kL_0}{2\pi}\right)} \tag{69}$$

$$C = B\exp\left[-\frac{a\gamma_{LA}}{E_0\tan\alpha\sin\alpha}\left(\cos\theta_0 + \cos\alpha\frac{kL_0}{2\pi}\right) - 1\right]. \tag{70}$$

6.3. Analysis of rough profiles

In this section, a patterned rough surface will be analyzed. Consider a periodic sawtooth profile with a distance between asperities d and width a, as shown in figure 8. Let us assume that the probability of the interface remaining composite, p, decreases exponentially with distance between asperities according to equation (67) (Nosonovsky and Bhushan 2006a). The roughness factor for the homogeneous interface, on the basis of equation (7), is given by

$$R_f = \frac{d + a/\cos\alpha}{d + a} = \frac{\phi + 1/\cos\alpha}{\phi + 1}. \tag{71}$$

The total fraction of valleys which are covered with liquid (homogeneous interface) is given by $1-p$, whereas the fraction of the valleys which have air pockets (composite interface) is given by p, obtained from equation (67). Based on this, the fractional areas are given by

$$f_{SL} = \frac{(1-p)(d + a/\cos\alpha)}{(1-p)(d + a/\cos\alpha) + p(d + a)} = \frac{(1-p)(\phi + 1/\cos\alpha)}{(1-p)(\phi + 1/\cos\alpha) + p(\phi + 1)} \tag{72}$$

$$f_{LA} = \frac{p(d + a)}{(1-p)(d + a/\cos\alpha) + p(d + a)} = \frac{p(\phi + 1)}{(1-p)(\phi + 1/\cos\alpha) + p(\phi + 1)}. \tag{73}$$

Substituting equations (71)–(73) into equation (12) yields the expression for the contact angle

$$\cos\theta = \frac{(1-p)(\phi + 1/\cos\alpha)^2\cos\theta_0 - p(\phi + 1)^2}{(1-p)(\phi + 1/\cos\alpha)(\phi + 1) + p(\phi + 1)^2}. \tag{74}$$

The results for the contact angle as a function of ϕ are presented in figure 10(a). It is observed that higher roughness (lower ϕ) corresponds to higher contact angles (Nosonovsky and Bhushan 2006a).

Comparison of the models, based on equations (6) (homogeneous interface), (12) (solid–liquid–air composite interface), and (74) (stochastic interface) is presented in figure 10(b). It is observed that for high roughness (small ϕ), $R_f\cos\theta_0 > 1$ and all three models predict $\theta = 180°$. However, for a higher distance between the asperities (higher ϕ), the composite interface model, which does not account for the possibility of destabilization, still predicts $\theta = 180°$, if $\theta_0 + \alpha > 180°$, whereas the homogeneous interface model predicts a rapid decrease of θ down to the value of θ_0, due to a decreasing roughness factor. The stochastic model yields the values of the contact angle close

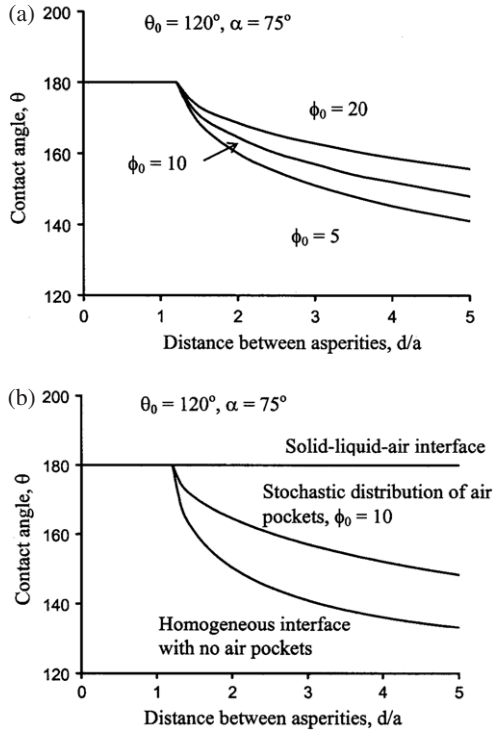

Figure 10. (a) Contact angle as a function of distance between asperities for the stochastic model. (b) Comparison of the interface with no air pockets, composite liquid–air interface and stochastic distribution of air pockets (Nosonovsky and Bhushan 2006a).

to the composite interface model for short distances between the asperities (small ϕ); however, with increasing ϕ, the probability of destabilization of the composite interface grows, and eventually the values of the contact angle approach those predicted by the homogeneous interface model.

6.4. Effect of gravity

In the preceding analysis we ignored the effect of gravity by assuming that the gravity force is small compared to the surface tension forces. However, for big droplets this assumption may not be correct. If the weight of a droplet exceeds the vertical component of the total surface tension force at the triple line, a droplet, suspended at the tops of the asperities, will collapse (Extrand 2002). Thus a maximum critical size of the droplet $R_{\max}$ exists, above which the droplet cannot remain suspended on the tops of the asperities. Let us investigate how this maximum size depends on the period of asperities l. Consider a rough surface with roughness period l and amplitude $\hat{z}$, which corresponds to maximum droplet size $R_{\max}$. The weight of the droplet is proportional to its volume and to the third power of $R_{\max}$:

$$W \propto R_{\max}. \tag{75}$$

For the maximum value of droplet radius, the weight is equal to the total vertical component of the surface tension, proportional to the surface tension times the cosine of the contact angle times the total perimeter of the triple lines:

$$W \propto \gamma_{SL} t N \cos\theta \tag{76}$$

where N is the number of asperities under the droplet (Nosonovsky and Bhushan 2006b).

Consider another rough surface with period αl and amplitude $\alpha\hat{z}$, which has the same roughness factor and the same contact angle. The length of the triple line for each asperity will be αt. The number of asperities under the droplet is proportional to the second power of $R_{\max}$ divided by the second power of α

$$N \propto R_{\max}^2/\alpha^2. \tag{77}$$

Combining equations (75)–(77) yields

$$R_{\max} \propto 1/\alpha. \tag{78}$$

This result suggests that with increasing asperity size the ability of a rough surface to form the composite interface decreases and larger droplets collapse. Therefore, smaller asperities make a composite interface more likely, due to gravity. Increasing the droplet size has the same effect as increasing the period of roughness (Nosonovsky and Bhushan 2006b).

7. Hierarchical roughness and stability of the composite interface

Although there is a significant literature about the lotus effect, and numerous attempts to produce artificial biomimetic roughness-induced hydrophobic surfaces have been made (Yost *et al* 1995, Shibuichi *et al* 1996, Onda *et al* 1996, Feng *et al* 2002, Erbil *et al* 2003, Patankar 2004a, 2004b, Cheng *et al* 2005, Sun *et al* 2005, Wang *et al* 2006), many details of the mechanism of roughness-induced non-wetting are still not well understood. In particular, it is not clear why the lotus leaf and other natural hydrophobic surfaces have a multiscale (or hierarchical) roughness structure, that is, nanoscale bumps superimposed over microscale asperities. Gao and McCarthy (2006) recently suggested that multiscale roughness affects the kinetics of droplet motion and the Laplace pressure at which water intrudes between the bumps. In the present study we investigate the effect of the multiscale roughness upon stability of the roughness-induced hydrophobic interface.

Wetting of a solid by a liquid is characterized by the contact angle, which is the angle between the solid–air and the liquid–air interfaces. The greater the contact angle, the more hydrophobic the material. The value of the contact angle is usually greater when the liquid is added (so-called advancing contact angle) than when it is removed (receding contact angle). The difference between the advancing and receding contact angle constitutes the contact angle hysteresis. The contact angle hysteresis is related to energy barriers, which a liquid droplet should overcome during its flow along a solid surface, and thus characterizes resistance to the flow. The lower the adhesion of a liquid droplet to the solid; the smaller the energy barriers, the lower the value of contact angle hysteresis, and the easier it is for the droplet to flow along the surface.

Several mechanisms are responsible for superhydrophobicity of natural surfaces such as lotus leaves. First, these surfaces are coated with wax, which is hydrophobic itself (with values of contact angle of about 103°, Kamusewitz *et al* 1999),

Second, they have a complicated geometrical structure with bumps or asperities (in the case of plant leaves called *papillae*) on the microscale (for the leaf of lotus the typical papilla size is of the order of 10 μm) covered with much smaller nanoscale bumps or nanometer-scale structures (Quéré 2005, Cheng *et al* 2005). In a similar manner, the legs of water striders are covered with a large number of oriented tiny hair (microsetae) with fine nanogrooves (Gao and Jiang 2004). Neinhuis and Barthlott (1997) suggested that hierarchical surfaces are less vulnerable against mechanical damage of nanostructures and therefore maintain functionality even after damage. Wagner *et al* (2003) showed that hierarchically structured surfaces are more readily able to repel water even if the surfaces tension is drastically reduced as compared to surfaces with only one length scale of roughening. This might be of importance in wetlands or other aquatic habitats where water is often polluted due to decaying plant material and other contaminations reducing surface tension (Wagner *et al* 2003). Herminghaus (2000) pointed out that certain self-affine profiles with multiscale roughness may result in superhydrophobic surfaces even for hydrophilic materials. However, theoretical explanation for the predominance of hierarchically structured surfaces in nature remains an important task.

It is believed that in order to be superhydrophobic, a rough surface should be able to maintain a composite interface with air pockets or bubbles trapped in the valleys between the asperities (Johnson and Dettre 1964, Marmur 2003, Patankar 2003, Lafuma and Quéré 2003), as opposed to a homogeneous solid–liquid interface. In many cases both a composite interface and the homogeneous interface may exist for the same surface; however, only a composite interface provides the required superhydrophobic properties. Furthermore, a composite interface is much less stable than a homogeneous interface, and it may be destroyed by liquid filling the valleys between asperities to form a homogeneous interface, whereas the opposite transition has never been observed (Quéré 2005). The mechanisms of this transition have been the subject of intensive investigation in recent years (Marmur 2003, Lafuma and Quéré 2003, Cheng *et al* 2005, Nosonovsky and Bhushan 2006a, Nosonovsky 2007a). Among factors suggested to affect the transition are the effects of the weight and curvature of the droplet. For small droplets, surface effects dominate over the gravity and the latter is hardly responsible for the transition, while curvature of the droplet may be responsible. The above suggests that stability of a composite interface is a key issue for the design of roughness-induced superhydrophobic surfaces. In this paper we formulate a geometrical stability criterion, and then investigate typical two-dimensional and three-dimensional surfaces with roughness at several scale levels. We show that a multiscale (hierarchical) roughness may enhance the stability of a composite interface.

7.1. Stability of a composite interface and hierarchical roughness

Spreading of liquid through porous media with a periodic geometry has been studied by several authors (Sharma and Ross 1991, Tsori 2006); however, stability of the composite interface has not been studied in detail in the literature. In this section, a geometrical stability condition for a composite interface will be formulated based on free energy minimization using the Lagrange method to find a minimum of a function of several variables with constraints. First, we will formulate the extremum criterion and show that it leads to the well-known Young equation, and then a stability criterion will be derived mathematically and its physical meaning will be discussed.

The liquid–air interface is at equilibrium if the free energy of the solid–liquid–air system reaches its minimum. In order to find local conditional minima of the free surface energy $W = A_{\mathrm{SL}}\gamma_{\mathrm{SL}} + A_{\mathrm{SA}}\gamma_{\mathrm{SA}} + A_{\mathrm{LA}}\gamma_{\mathrm{LA}}$ with the constant volume constraint $V = V_0$, the Lagrange function is constructed

$$L(A_{\mathrm{SL}}, A_{\mathrm{SA}}, A_{\mathrm{LA}}, V, \lambda) = A_{\mathrm{SL}}\gamma_{\mathrm{SL}} + A_{\mathrm{SA}}\gamma_{\mathrm{SA}} + A_{\mathrm{LA}}\gamma_{\mathrm{LA}} + p(V - V_0) \tag{79}$$

where A_{SL}, A_{SA}, A_{LA} are areas of the solid–liquid, solid–air and liquid–air interfaces and γ_{SL}, γ_{SA}, γ_{LA} are corresponding free energies, V_0 is the volume and p is the Lagrange multiplier (Greenberg 1978), having the dimension of pressure. The corresponding change of L is given by

$$\delta L = \delta A_{\mathrm{SL}}\gamma_{\mathrm{SL}} + \delta A_{\mathrm{SA}}\gamma_{\mathrm{SA}} + \delta A_{\mathrm{LA}}\gamma_{\mathrm{LA}} + \lambda\delta V + \delta p(V - V_0). \tag{80}$$

Note, that the arguments of L are interdependent with $\delta A_{\mathrm{SL}} = -\delta A_{\mathrm{SA}}$ whereas δA_{LA} consists of two terms, $\delta A_{\mathrm{LA}} = \delta A_{\mathrm{LAT}} + \delta A_{\mathrm{LAV}}$. The first term, δA_{LAT}, is due to a change in position of the triple line (line of contact between solid, liquid, and air) and the second, δA_{LAV}, is due to a change in the shape of the liquid–air interface. Furthermore, $\delta A_{\mathrm{LAT}} = \delta A_{\mathrm{SL}} \cos\theta$ from geometrical considerations (Nosonovsky 2007a).

Suppose the shape of the liquid–air interface is given parametrically by vector $\vec{r}(u, v)$, where u and v are parameters which uniquely characterize any point at a surface, and the shape changes slightly

$$\breve{\vec{r}}(u, v) = \vec{r}(u, v) + \overrightarrow{\delta r}(u, v). \tag{81}$$

The change due to the shape of the liquid–air interface is given by the area of an element of the liquid–air interface $A(u, v)\,\mathrm{d}u\,\mathrm{d}v$ times the normal displacement multiplied by the sum of principal radii of curvature $\vec{n}\overrightarrow{\delta r}(1/R_1 + 1/R_2)$, where $\vec{n}$ is the normal vector and R_1, R_2 are the principal radii of curvature

$$\delta A_{\mathrm{LAV}} = \iint_{A_{\mathrm{LA}}} \vec{n}\overrightarrow{\delta r}(1/R_1 + 1/R_2)A\,\mathrm{d}u\,\mathrm{d}v \tag{82}$$

where (Greenberg 1978)

$$A(u, v) = \left[\left(\frac{\partial\vec{r}}{\partial u}\right)^2\left(\frac{\partial\vec{r}}{\partial v}\right)^2 - \left(\frac{\partial\vec{r}}{\partial u}\frac{\partial\vec{r}}{\partial v}\right)^2\right]^{1/2}. \tag{83}$$

The change in volume is given by

$$\delta V = \iint_{A_{\mathrm{LA}}} \vec{n}\overrightarrow{\delta r}\,A\,\mathrm{d}u\,\mathrm{d}v. \tag{84}$$

Combining equations (82)–(84) and setting $\delta L(\delta A_{SL}, \delta \boldsymbol{r}, \delta V) = 0$ yields

$$\delta L = \delta A_{SL}\left[\cos\theta_0 - \frac{\gamma_{SA}-\gamma_{SL}}{\gamma_{LA}}\right]\gamma_{LA} + \iint_{A_{LA}} [\gamma_{LA}(1/R_1 + 1/R_2) + p]\vec{n}\,\overrightarrow{\delta r}\, A\,\mathrm{d}u\,\mathrm{d}v + \lambda\delta V \quad (85)$$

which results in three equations that should be satisfied simultaneously. The first is the Young equation for the contact angle θ_0, which should be satisfied at the points of the triple line:

$$\cos\theta_0 = \frac{\gamma_{SA}-\gamma_{SL}}{\gamma_{LA}}. \quad (86)$$

The second equation for the Lagrange multipliers $p = -\gamma_{LA}(1/R_1 + 1/R_2)$ is satisfied only if the curvature $1/R_1 + 1/R_2$ is a constant independent of u and v throughout the entire liquid–air interface (Nosonovsky 2007a). Physically, of course, this condition reflects Laplace pressure drop through a curved interface. The third equation is just the condition of constant volume $V = V_0$ (Nosonovsky 2007a).

In order for the extremum to be a local minimum (rather than a maximum) of W, the equilibrium should also satisfy the stability condition $\mathrm{d}^2W > 0$. Differentiating $W = A_{SL}\gamma_{SL} + A_{SA}\gamma_{SA} + A_{LA}\gamma_{LA}$ and using $\delta A_{LA} = \delta A_{SL}\cos\theta$ twice yields

$$\mathrm{d}^2W = \mathrm{d}^2A_{SL}\left[\cos\theta_0 - \frac{\gamma_{SA}-\gamma_{SL}}{\gamma_{LA}}\right]\gamma_{SL} + \mathrm{d}A_{LA}\,\mathrm{d}(\cos\theta) > 0. \quad (87)$$

We ignored the effect of the changing shape of the liquid–air interface (the term corresponding to δA_{LAV}), since it is known that $1/R_1 + 1/R_2 = \text{const}$ provides the minimum (rather than the maximum) liquid–air interface area condition and only the effect of moving the triple line is of interest for us. Using equation (86), which is satisfied at the equilibrium, and the fact that $\cos\theta$ decreases monotonically with θ at the domain of our interest, $0° < \theta < 180°$, yields (Nosonovsky 2007a)

$$\mathrm{d}A_{SL}\,\mathrm{d}\theta < 0. \quad (88)$$

In other words, in order for the interface to be stable, for advancing liquid (increasing A_{SL}) the value of the contact angle should decrease, whereas for receding liquid the contact angle should increase. Note also that for a liquid–air interface coming to the solid surface under the angle θ, an advance of the interface results in the change of energy

$$\begin{aligned}\mathrm{d}W &= \mathrm{d}A_{SL}(\gamma_{SL}-\gamma_{SA}) + \mathrm{d}A_{LA}\gamma_{LA}\\ &= \mathrm{d}A_{SL}(\gamma_{SL}-\gamma_{SA}) + \mathrm{d}A_{SL}\gamma_{LA}\cos\theta\\ &= \mathrm{d}A_{SL}\gamma_{LA}\left(-\frac{\gamma_{SA}-\gamma_{SL}}{\gamma_{LA}} + \cos\theta\right)\\ &= \mathrm{d}A_{SL}\gamma_{LA}(\cos\theta - \cos\theta_0). \end{aligned} \quad (89)$$

Thus, if $\theta > \theta_0$, the energy decreases and it is energetically profitable for the liquid to advance, whereas if $\theta < \theta_0$, the liquid would retreat. So, the physical meaning of equation (88) is that for a small advance/retreat of the liquid it should be more energetically profitable to return to the original position rather than continue to advance/retreat (Nosonovsky 2007a).

For a two-dimensional surface, since a change of angle $\mathrm{d}\theta$ is equal to the change of slope of the surface, it depends on the sign of curvature of the surface whether the configuration is stable or not. The convex (bumpy) surface leads to a stable interface, whereas a concaved (groovy) surface leads to an unstable interface. The liquid keeps spreading until both equations (86) and (88) are satisfied at the triple line and $1/R_1 + 1/R_2 = \text{const}$ at the liquid–air interface, provided the volume of the liquid is conserved.

In the next section, we will apply the stability criterion (equation (88)) to typical two-dimensional and three-dimensional surfaces with multiscale roughness.

7.2. Hierarchical roughness

In this section, we will consider several surfaces with nanoscale roughness superimposed over larger microscale pillars and will investigate the effect of concaved and convex nanoroughness upon the stability of a composite interface. We will study the case of an infinitely large reservoir of liquid on top of the pillars. In most applications, liquid droplets of finite size are in contact with a rough surface; however, the size of roughness details is small compared to the size of the droplets and for practical purposes droplet size can be considered infinite.

7.2.1. Two-dimensional roughness. Consider a two-dimensional structure with rectangular pillars of height h and width a separated by a distance b, covered with small semi-circular ridges and grooves of radius r (figure 11(a)). Since the distance between the pillars is small in comparison with the capillary length, and therefore the effect of gravity is negligible, we can assume that the liquid–air interface is a horizontal plane, and its position is characterized by the vertical coordinate z. The free energy is given by Nosonovsky (2007a)

$$\begin{aligned}W &= A_{SL}\gamma_{SL} + A_{SA}\gamma_{SA} + A_{LA}\gamma_{LA}\\ &= rL\gamma_{LA}(\sin\alpha - \alpha\cos\theta_0), \qquad 0 < z < h\end{aligned} \quad (90)$$

where $\alpha = a\cos((r-z)/r) + 2\pi N$ is the angle corresponding to vertical position of the interface z, N is the number of a ridge or groove, and L is length of the grooves in the y-direction, which is required based on the dimensional considerations. The dependence is presented in figure 11(b) for the cases of hydrophobic ($\theta_0 = 150°$) and hydrophilic ($\theta_0 = 30°$) materials for both the bumpy and the grooved surface. It is seen that for the bumpy surface there are many states of stable equilibrium (shown in figure 11(a) with dotted lines), separated by energy barriers, which correspond to every ridge, whereas for the grooved surface equilibrium states are unstable. Therefore, the ridges can pin the triple line and thus lead to a composite interface. In the case of a hydrophilic surface, each lower position of the equilibrium state corresponds to a lower value of W, therefore when the liquid advances from one equilibrium state to the next, the total energy decreases and thus liquid's advance is energetically profitable. When the liquid reaches the bottom of the valley and completely fills the space between the pillars forming a homogeneous interface, the total energy decreases dramatically by the value of

$$\Delta W = bL(\gamma_{SA} + \gamma_{LA} - \gamma_{SL}) = bL\gamma_{LA}(1 + \cos\theta_0). \quad (91)$$

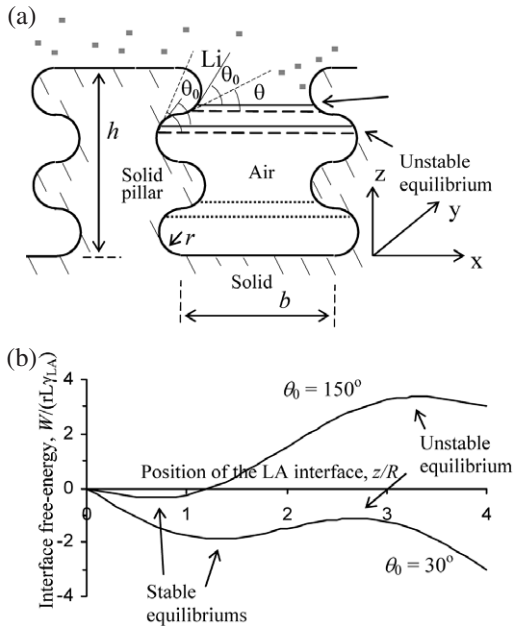

Figure 11. Two-dimensional pillars with semi-circular bumps/grooves. (a) Schematics of the structure. The bumps may pin the triple line, because an advance of the liquid–air (LA) interface results in decrease of the contact angle ($\theta < \theta_0$), making equilibrium stable. Grooves provide equilibrium positions which satisfy the Young equation; however, the equilibrium is unstable because an advance of the LA interface results in increase of the contact angle ($\theta > \theta_0$). (b) Energy profiles for configurations in figure 2(a) with bumps and grooves for hydrophilic ($\theta_0 = 30°$) and hydrophobic ($\theta_0 = 150°$) materials. Energy (normalized by $Lr\gamma_{LA}$) is shown as a function of vertical position of the interface z (normalized by the radius of bumps/grooves r). Bumps result in stable equilibria (energy minima), whereas grooves result in unstable equilibria (energy maxima) (Nosonovsky 2007a).

The opposite transition from a homogeneous interface to a composite interface requires a high activation energy ΔW and is thus unlikely, making the transition from a composite interface to a homogeneous interface irreversible. Since the distance between the pillars b is much greater than r, the energy barriers which separate the equilibrium states $2\pi r L\gamma_{LA}\cos\theta_0$ are relatively small compared with ΔW, and a low activation energy is required for the liquid to spread and propagate from one equilibrium state to the other (Nosonovsky and Bhushan 2007a, 2007b).

Since the change of angle $d\theta$ for a two-dimensional surface is equal to the change of surface slope, based on equation (88), whether the configuration is stable or not depends upon the sign of curvature of the surface. A convex (bumpy) surface leads to a stable interface, whereas a concaved (grooved) surface leads to an unstable interface. The liquid keeps spreading until both equations (8) and (10) are satisfied at the triple line and $1/R_1 + 1/R_2 = \text{const}$ at the liquid–air interface, provided the volume of the liquid is conserved, which is the case for a slow thermodynamic process.

7.2.2. Three-dimensional pillars with ridges and grooves. Consider now a three-dimensional structure with circular pillars of height h and radius R separated by distance b and

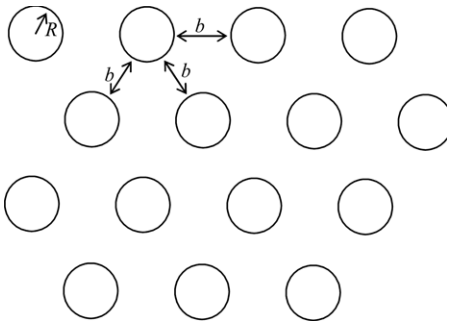

Figure 12. Schematics of the spatial distribution of three-dimensional pillars with semi-circular bumps/grooves upon a surface (Nosonovsky 2007a).

distributed hexagonally with a density of $\eta = 2/[\sqrt{3}(2R+b)^2]$ pillars per unit area, covered with small ridges and grooves of radius r (figure 11(a)). Similarly to the preceding section, the free energy per area S is given by the circumference of a pillar $2\pi R$ times the number of pillars ηS times $r\gamma_{LA}(\sin\alpha - \alpha\cos\theta_0)$

$$W = 2\pi R\eta S r\gamma_{LA}(\sin\alpha - \alpha\cos\theta_0), \qquad 0 < z < h. \quad (92)$$

The similarity between equations (90) and (92) is noted, both energy profiles are different only in their normalization constant, so the dependence of the free energy upon the position of the interface is presented in figure 11(b) for the case of two-dimensional pillars has qualitatively the same profile as for the case of three-dimensional pillars. In a similar manner to the case of two-dimensional pillars, the ridges can pin the triple line (Nosonovsky 2007a).

7.2.3. Three-dimensional surface. In the previous sections we considered two-dimensional nanoscale ridges and grooves superimposed over two- and three-dimensional pillars. Real superhydrophobic surfaces, such as plant leaves, are three-dimensional with three-dimensional nanobumps. For three-dimensional surfaces, the shape of the liquid–air interface may be quite complex and thus the stability of the composite interface is difficult to analyze. In order to consider a three-dimensional configuration which allows for a plane horizontal liquid–air interface we will investigate a surface composed of circular pillars of height h and radius R separated by distance b with the density of $\eta = 2/[\sqrt{3}(2R + b)^2]$ pillars per unit area (following the hexagonal distribution pattern shown in figure 12), which are formed of layers of small spheres of radius r, packed according to the hexagonal pattern (figure 13(a)). The packing density of the spheres is equal to $1/(2\sqrt{3}r^2)$ spheres per unit area in every horizontal layer. The liquid–air interface area is now given by the total flat area of the surface, A_0, minus the cross-sectional area of spheres under water. The latter is given by A_0 times the pillar density η times the pillar area πR^2 times the packing density of the spheres $1/(2\sqrt{3}r^2)$ times the cross-sectional area of individual sphere under water, $\pi(r\sin\alpha)^2$, which yields (Nosonovsky 2007a)

$$A_{LA} = A_0\left(1 - \frac{\eta\pi^2 R^2\sin^2\alpha}{2\sqrt{3}}\right). \quad (93)$$

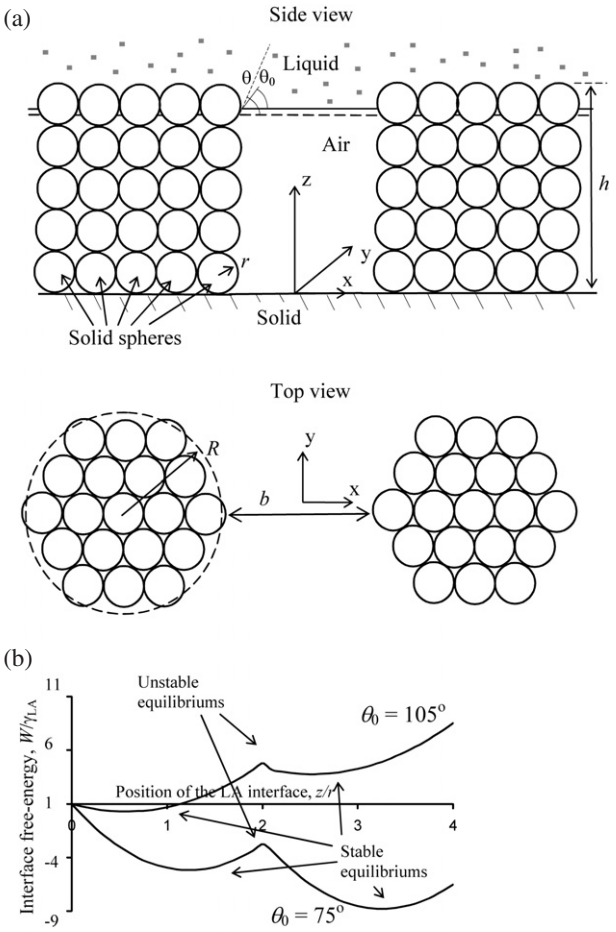

Figure 13. Three-dimensional pillars consisting of small solid spheres. (a) Schematics of the structure. (b) Energy (normalized by $A_0\gamma_{LA}$) as a function of vertical position of the interface z (normalized by the radius of bumps/grooves r) for $\pi^2R^2/(2\sqrt{3}r^2) = 1$ (Nosonovsky 2007a).

The solid–liquid interface area is equal to the total surface area of the spheres under water, which is given by the number of spheres $\eta A_0\pi^2R^2/(2\sqrt{3}r^2)$ times the surface area of the spheres multiplied by the number of layers $4\pi r^2N$ plus the area of the spheres in the layer, which is only partially under water, $\pi(z^2 + 2z(2r - z))$:

$$A_{SL} = \frac{\eta A_0\pi^2R^2}{2\sqrt{3}r^2}[4r^2N + (z^2 + 2z(2r - z))]. \qquad (94)$$

Using $\sin^2\alpha = 1-\cos^2\alpha = 1-((r-z)/r)^2 = 2z/r-(z/r)^2$, the free energy is now given by

$$W = A_{LA}\gamma_{LA} + A_{SL}(\gamma_{LA} - \gamma_{SA}) = \gamma_{LA}(A_{LA} + A_{SL}\cos\theta_0)$$
$$= A_0\gamma_{LA}\left(1 - \frac{\eta\pi^2R^2}{2\sqrt{3}}\{2z/r - (z/r)^2 - [4\pi N + (z/r)^2 + 2(z/r)(2 - z/r)]\cos\theta_0\}\right). \qquad (95)$$

The dependence of the free energy, normalized by $A_0\gamma_{LA}$, upon the vertical position z is presented in figure 13(b) for the cases of hydrophobic ($\theta_0 = 105°$) and hydrophilic ($\theta_0 = 75°$) materials (Nosonovsky 2007a).

7.3. Results and discussion

We studied three different surface profiles with large-scale pillars and small-scale roughness superimposed over the pillars. It is observed from figures 11(b) and 13(b) that for both the hydrophobic and hydrophilic materials a convex surface leads to stable equilibria, whereas a concaved surface leads to unstable equilibria. Therefore, a convex small-scale roughness can pin the liquid–air interface even in the case of a hydrophilic material. This may be important for producing reliable superhydrophobic surfaces, since the factors destabilizing the liquid–air interface, such as nanodroplet condensation (Cheng *et al* 2005, Oner and McCarthy 2000), chemical surface heterogeneity (Checco *et al* 2003), and capillary waves (Nosonovsky and Bhushan 2006a) are scale-dependent and therefore multiscale roughness is required to control the stability.

An experiment suggesting that the sign of curvature is indeed important for hydrophobicity was conducted by Sun *et al* (2005). They produced both a positive and a negative replica of a lotus leaf surface by nanocasting, using poly(dimethylsiloxane), which has a contact angle with water of about 105°. This value is close to the contact angle of the wax which covers lotus leaves (about 103°, Kamusewitz *et al* 1999). The positive and negative replicas have the same roughness factor and thus should produce the same contact angle in the case of a homogeneous interface; however, the values of the surface curvature are opposite. The value of contact angle for the positive replica was found to be 160° (same as for lotus leaf), while for the negative replica it was only 110°. This result suggests that the high contact angle of the lotus leaf is due to the composite rather than homogeneous interface and that the sign of surface curvature indeed plays a critical role for formation of the composite interface.

Natural and successful artificial superhydrophobic surfaces exhibit hierarchical multiscale roughness. Thus, the lotus leaf has microscale bumps (papillae) with a typical height and radius of 10–20 μm, which are covered with hydrophobic paraffin wax. Upon these bumps much smaller nanobumps are found, with typical submicron sizes. Artificial biomimetic superhydrophobic surfaces should also have multiscale roughness.

To summarize, biomimetic superhydrophobic surfaces should satisfy the following requirements: they should have hydrophobic coating, high roughness factors, providing high contact angle, and the ability to form a composite interface. To achieve a stable composite interface, a hierarchical roughness structure with nanoscale bumps upon microscale asperities and valleys is required.

The mechanism of roughness-induced hydrophobicity is complicated and involves effects at various scale ranges. For most superhydrophobic surfaces it is important that a composite solid–liquid–air interface is formed. A composite interface dramatically decreases the area of contact between liquid and solid and, therefore, decreases the adhesion of a liquid droplet to the solid surface and contact angle hysteresis. Formation of a composite interface is also a multiscale phenomenon which depends upon relative sizes of the liquid droplet and roughness details. The composite

interface is fragile, since transition to a homogeneous interface is irreversible. Therefore, the stability of a composite interface is crucial for superhydrophobicity and should be addressed for successful development of superhydrophobic surfaces. We have demonstrated that multiscale roughness can help to resist destabilization, with convex surfaces pinning the interface and thus leading to stable equilibrium and preventing filling of the gaps between the pillars even in the case of a hydrophilic material. The effect of roughness on wetting is scale dependent and mechanisms that lead to destabilization of a composite interface are also scale dependent. To effectively resist these scale-dependent mechanisms, a multiscale roughness is required. Such multiscale roughness was found in natural and successful artificial superhydrophobic surfaces.

8. Cassie–Wenzel transition

8.1. The Cassie–Wenzel transition and the contact angle hysteresis

It is known from experimental observations, that the transition from the Cassie to the Wenzel state is an irreversible event (Lafuma and Quéré 2003, Barbieri *et al* 2007, Bhushan *et al* 2007). Whereas such a transition can be induced, for example, by applying pressure or force to the droplet (Barbieri *et al* 2007), by electrical voltage (Krupenkin *et al* 2004, Bahadur and Garimella 2007), by light for a photocatalytic texture (Feng *et al* 2004), and by vibration (Bormashenko *et al* 2007), the opposite transition has never been observed, although there is no apparent reason for that. Several approaches have been proposed for investigation of the Cassie–Wenzel transition. Lafuma and Quéré (2003) suggested that the transition takes place when the net surface energy of the Wenzel state becomes equal to that of the Cassie state, or, in other words, when the contact angle predicted by the Cassie equation is equal to that predicted by the Wenzel equation. They noticed that in certain case the transition does not occur even when it is energetically profitable, and considered such a Cassie state metastable. Extrand (2003) suggested that the weight of the droplet is responsible for the transition and proposed the contact line density model, according to which the transition takes place when the weight exceeds the surface tension force at the triple line. Patankar (2004a) suggested that which of the two states is realized may depend upon how the droplet was formed, that is upon the history of the system. Quéré (2005) also suggested that the curvature of the droplet (which depends upon the pressure difference between the inside and outside of the droplet) governs the transition. Nosonovsky and Bhushan (2006a) suggested that the transition is a dynamic process of destabilization and identified possible destabilizing factors. It has been also suggested that curvature of multiscale roughness defines the stability of the Cassie state (Nosonovsky and Bhushan 2007a, 2007b, Nosonovsky 2007a) and that the transition is a gradual stochastic process (Nosonovsky and Bhushan 2005, Ishino and Okumura 2006, Bormashenko *et al* 2007). Numerous experimental results support many of these approaches; however, it is not clear which particular mechanism prevails.

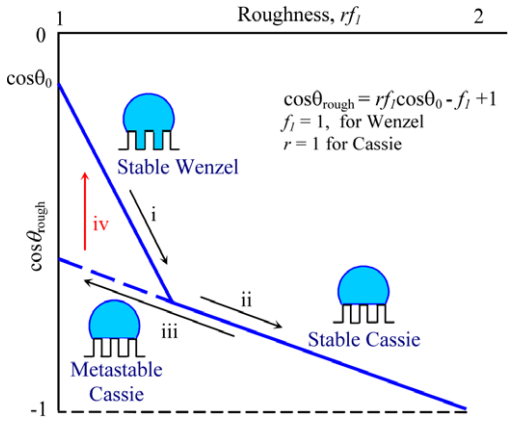

Figure 14. Wetting hysteresis for a superhydrophobic surface. Contact angle as a function of roughness. The stable Wenzel state (i) can transform into the stable Cassie state with increasing roughness (ii). The metastable Cassie state (iii) can abruptly transform (iv) into the stable Wenzel state. The transition (i)–(ii) corresponds to equal free energies for the Wenzel and Cassie states, whereas the transition (iv) corresponds to a significant energy dissipation and thus it is irreversible.

There is an asymmetry between the wetting and dewetting processes, since droplet nucleation requires less energy than vapor bubble nucleation (cavitation). During wetting, which involves creation of the solid–liquid interface, less energy is released than the amount required for dewetting or destroying the solid–liquid interface due to adhesion hysteresis. Adhesion hysteresis is one of the factors that leads to the contact angle hysteresis and it also results in the hysteresis of the Wenzel–Cassie state transition. Figure 14 shows the contact angle of a rough surface as a function of surface roughness (which is measured for the Wenzel regime by $r > 1$, $f_1 = 1$ and for the Cassie regime by $f_1 > 1$, $r = 1$). It is noted that at a certain point, given by $r = f_1 + (1 - f_1)/\cos\theta_1$, the lines corresponding to the Wenzel and Cassie regimes intersect. This point corresponds to an equal net energy of the Cassie and Wenzel states. For a lower roughness (e.g. a larger pitch between the pillars) the Wenzel state is more energetically profitable, whereas for a higher roughness the Cassie state is more energetically profitable.

It is observed from figure 14 that an increase in roughness may lead to a transition between the Wenzel and Cassie regimes at the intersection point. With decreasing roughness, the system is expected to transit to the Wenzel state. However, experiments show (Bhushan *et al* 2007, Barbieri *et al* 2007) that, despite the energy of the Wenzel state being lower than that of the Cassie state, the transition does not necessarily occur and the droplet may remain in the metastable Cassie state. This is because there are energy barriers associated with the transition, which occurs due to destabilization by dynamic effects (such as waves and vibration).

In order to understand the contact angle hysteresis and transition between the Cassie and Wenzel states, the shape of the free surface energy profile can be analyzed. The free surface energy of a droplet upon a smooth surface as a function of the contact angle has a distinct minimum, which corresponds to the most stable contact angle. As shown in

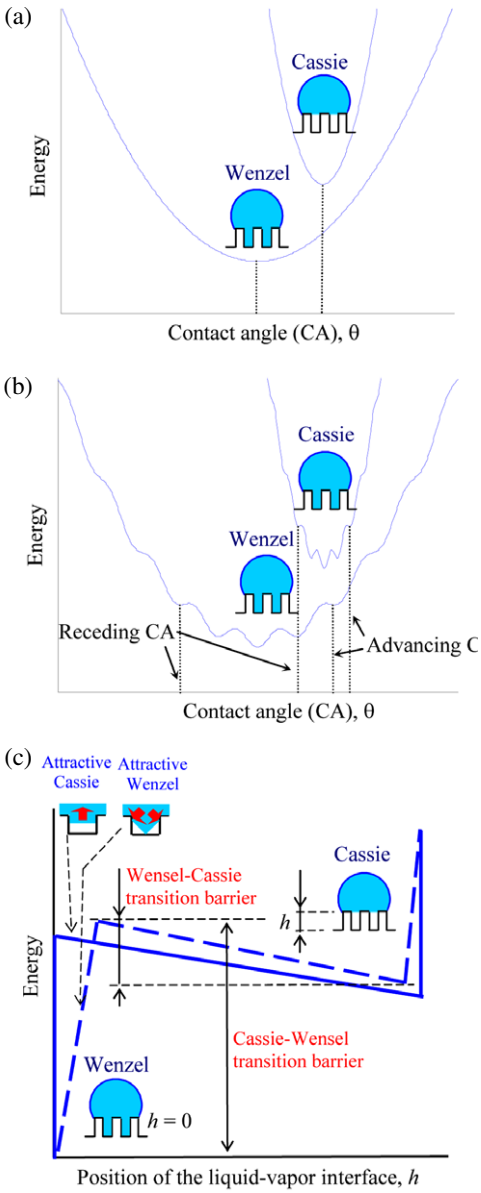

Figure 15. Schematics of net free energy profiles. (a) Macroscale description; energy minima correspond to the Wenzel and Cassie states. (b) Microscale description with multiple energy minima due to surface texture. The largest and smallest values of the energy minimum correspond to the advancing and receding contact angles. (c) The origin of the two branches (Wenzel and Cassie) is found when a dependence of energy upon h is considered for the microscale description (solid line) and nanoscale imperfection (dashed line); based on Nosonovsky and Bhushan (2006a). When nanoscale imperfection is introduced, it is observed that the Wenzel state corresponds to an energy minimum and the energy barrier for the Wenzel–Cassie transition is much smaller than for the opposite transition.

figure 15(a), the macroscale profile of the net surface energy allows us to find the contact angle (corresponding to energy minima), but it fails to predict the contact angle hysteresis and Cassie–Wenzel transition, which is governed by micro- and nanoscale effects. As soon as the microscale substrate roughness is introduced, the droplet shape can no longer be considered as an ideal truncated sphere, and energy profiles have multiple energy minima corresponding to the location of the pillars (figure 15(b)). The microscale energy profile (solid line) has numerous energy maxima and minima due to the surface micropattern. While exact calculation of the energy profile for a 3D droplet is complicated, a qualitative shape may be obtained by assuming a periodic sinusoidal dependence (Johnson and Dettre 1964) superimposed upon the macroscale profile, as shown in figure 15(b). Thus the advancing and receding contact angles can be identified as the maximum and minimum possible contact angles corresponding to minimum energy points. However, the transition between the Wenzel and Cassie branches still cannot be explained. Note also that figure 15(b) explains qualitatively the hysteresis due to the kinetic effect of the pillars but not the inherited adhesion hysteresis, which is characterized by the molecular scale length and cannot be captured by the microscale model.

The energy profile as a function of the contact angle does not provide any information on how the transition between the Cassie and Wenzel states occurs, because these two states correspond to completely isolated branches of the energy profile in figures 15(a) and (b). However, the energy may depend not only upon the contact angle but also upon micro-/nanoscale parameters, such as for example the vertical position of the liquid–vapor interface under the droplet, h (assuming that the interface is a horizontal plane), or similar geometrical parameters (assuming a more complicated shape of the interface). In order to investigate the Wenzel–Cassie transition, the dependence of the energy upon these parameters should be studied. We assume that the liquid–vapor interface under the droplet is a flat horizontal plane. When such a vapor layer thickness or the vertical position of the liquid–vapor interface, h, is introduced, the energy can be studied as a function of droplet shape, the contact angle, and h (figure 15(c)). For an ideal situation the energy profile has an abrupt minimum at the point corresponding to the Wenzel state, which corresponds to the sudden net energy change due to destroyed solid–vapor and liquid vapor interfaces ($\gamma_{SL} - \gamma_{SV} - \gamma_{LV} = -\gamma_{LV}(\cos\theta + 1)$ times the interface area) (figure 15(c)). In a more realistic case, the liquid–vapor interface cannot be considered horizontal due to nanoscale imperfection or dynamic effects such as capillary waves (Nosonovsky and Bhushan 2006a). A typical size of the imperfection is much smaller than the size of the details of the surface texture and thus belongs to the molecular scale level. The height of the interface, h, can now be treated as an average height. The energy dependence upon h is now not as abrupt as in the idealized case. For example, for the 'triangular' shape as shown in figure 15(c), the Wenzel state may become the second attractor for the system. It is seen that there are two equilibria which correspond to the Wenzel and Cassie states, with the Wenzel state corresponding to a much lower energy level. The energy dependence upon h governs the transition between the two states and it is observed that a much larger energy barrier exists for the transition from Wenzel to Cassie than for the opposite transition. This is why the first transition has never been observed experimentally.

To summarize, we showed that the contact angle hysteresis and Cassie–Wenzel transition cannot be determined

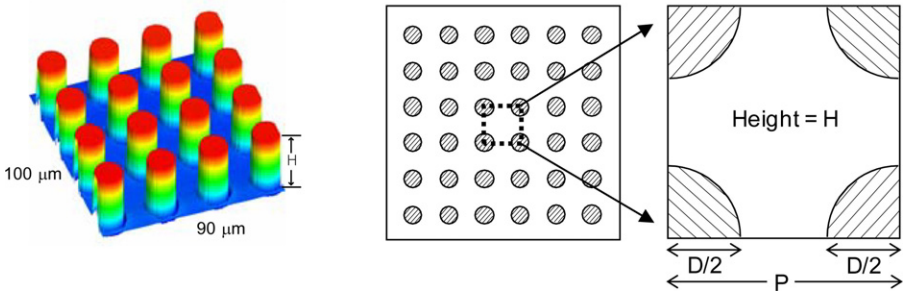

Figure 16. Optical profiler image and schematic of the patterned surface (Jung and Bhushan 2007).

from the macroscale equations and are governed by micro- and nanoscale phenomena. Our theoretical arguments are supported by our experimental data on micropatterned surfaces.

8.2. Experimental study of the Cassie–Wenzel transition

Bhushan and Jung (2007) studied two series of patterned Si surfaces covered with a monolayer of hydrophobic tetrahydroperfluorodecyltrichlorosilane (contact angle with a nominally flat surface, $\theta_0 = 109°$; advancing and receding contact angles $\theta_{adv0} = 116°$ and $\theta_{rec0} = 82°$), formed by flat-top cylindrical pillars. Series 1 had pillars with diameter $D = 5$ μm, height $H = 10$ μm, and pitch values $P = (7, 7.5, 10, 12.5, 25, 37.5, 45, 60,$ and $75)$ μm, while Series 2 had $D = 14$ μm, $H = 30$ μm, $P = (21, 23, 26, 35, 70, 105, 126, 168,$ and $210)$ μm (figure 16). It is convenient to introduce the spacing factor $S_f = D/P$ (Nosonovsky and Bhushan 2007a, 2007b). The contact angle and contact angle hysteresis of millimeter-sized water droplets upon the samples were measured. In addition, contact angle and the Wenzel–Cassie transition during evaporation in ambient and evaporation/condensation of microscale droplets in an environment scanning electron microscope (ESEM) were studied (figure 17). We found that the contact angle hysteresis involves two terms: the term $S_f^2(\pi/4)(\cos\theta_{adv0} - \cos\theta_{rec0})$ corresponding to the adhesion hysteresis (which is found even at a nominally flat surface and is a result of molecular-scale imperfection) and the term $H_r \propto D/P^2$ corresponding to microscale roughness and proportional to the edge line density. Thus the contact angle hysteresis is given, based on equation (53), by Bhushan *et al* (2007)

$$\cos\theta_{adv} - \cos\theta_{rec} = \frac{\pi}{4} S_f^2(\cos\theta_{adv0} - \cos\theta_{rec0}) + H_r. \quad (96)$$

The droplet radius, R, at the Cassie–Wenzel transition was found to be proportional to P/D (or P/H) (figure 18), which suggests that the transition is a linear '1D' phenomenon and that neither droplet droop (that would involve P^2/H) nor droplet weight (that would involve R^3) are responsible for the transition, but rather linear geometric relations are involved. Note that the experimental values approximately correspond to the values of the ratio $RD/P = 50$ μm or the total area of the pillar tops under the droplet $(\pi D^2/4)\pi R^2/P^2 = 6200$ μm^2.

Besides the contact angle hysteresis, the asymmetry of the Wenzel and Cassie states is the result of the wetting/dewetting asymmetry. While a fragile metastable Cassie state is often observed, as well as its transition to the Wenzel state, the opposite transition never happens. Using equations (6) and (9), the contact angle with the patterned surfaces is given by Bhushan and Jung (2007)

$$\cos\theta = (1 + 2\pi S_f^2)\cos\theta_0 \qquad \text{(Wenzel state)} \qquad (97)$$

$$\cos\theta = \frac{\pi}{4} S_f^2(\cos\theta_0 + 1) - 1 \qquad \text{(Cassie state).} \qquad (98)$$

For a perfect macroscale system, the transition between the Wenzel and Cassie states should occur only at the intersection of the two regimes (the point at which the contact angle and net energies of the two regimes are equal, corresponding to $S_f = 0.51$). It is observed, however, that the transition from the metastable Cassie state to the stable Wenzel state occurs at much lower values of the spacing factor $0.083 < S_f < 0.111$. As shown in figure 19(a), the stable Wenzel state (i) can transform into the stable Cassie state with increasing S_f (ii). The metastable Cassie state (iii) can abruptly transform (iv) into the stable Wenzel state. The transition (i)–(ii) corresponds to equal Wenzel and Cassie states free energies, whereas the transition (iv) corresponds to a Wenzel energy much lower than the Cassie energy and thus involves significant energy dissipation and is irreversible. The solid and dashed straight lines correspond to the values of the contact angle, calculated from equations (97) and (98) using the contact angle for a nominally flat surface, $\theta_0 = 109°$. The two series of experimental data are shown with squares and diamonds.

Figure 19(b) shows the values of the advancing contact angle plotted against the spacing factor. The solid and dashed straight lines correspond to the values of the contact angle for the Wenzel and Cassie states, calculated from equations (97) and (98) using the advancing contact angle for a nominally flat surface, $\theta_{adv0} = 116°$. It is observed that the calculated values underestimate the advancing contact angle, especially for big S_f (small distance between the pillars or pitch P). This is understandable, because the calculation takes into account only the effect of the contact area and ignores the effect of roughness and edge line density (it corresponds to $H_r = 0$ in equation (96)), while this effect is more pronounced for high pillar density (big S_f). In a similar manner, the contact angle is underestimated for the Wenzel state, since the pillars constitute a barrier to the advancing droplet.

Figure 19(c) shows the values of the contact angle after the transition took place (dimmed blue squares and diamonds), as

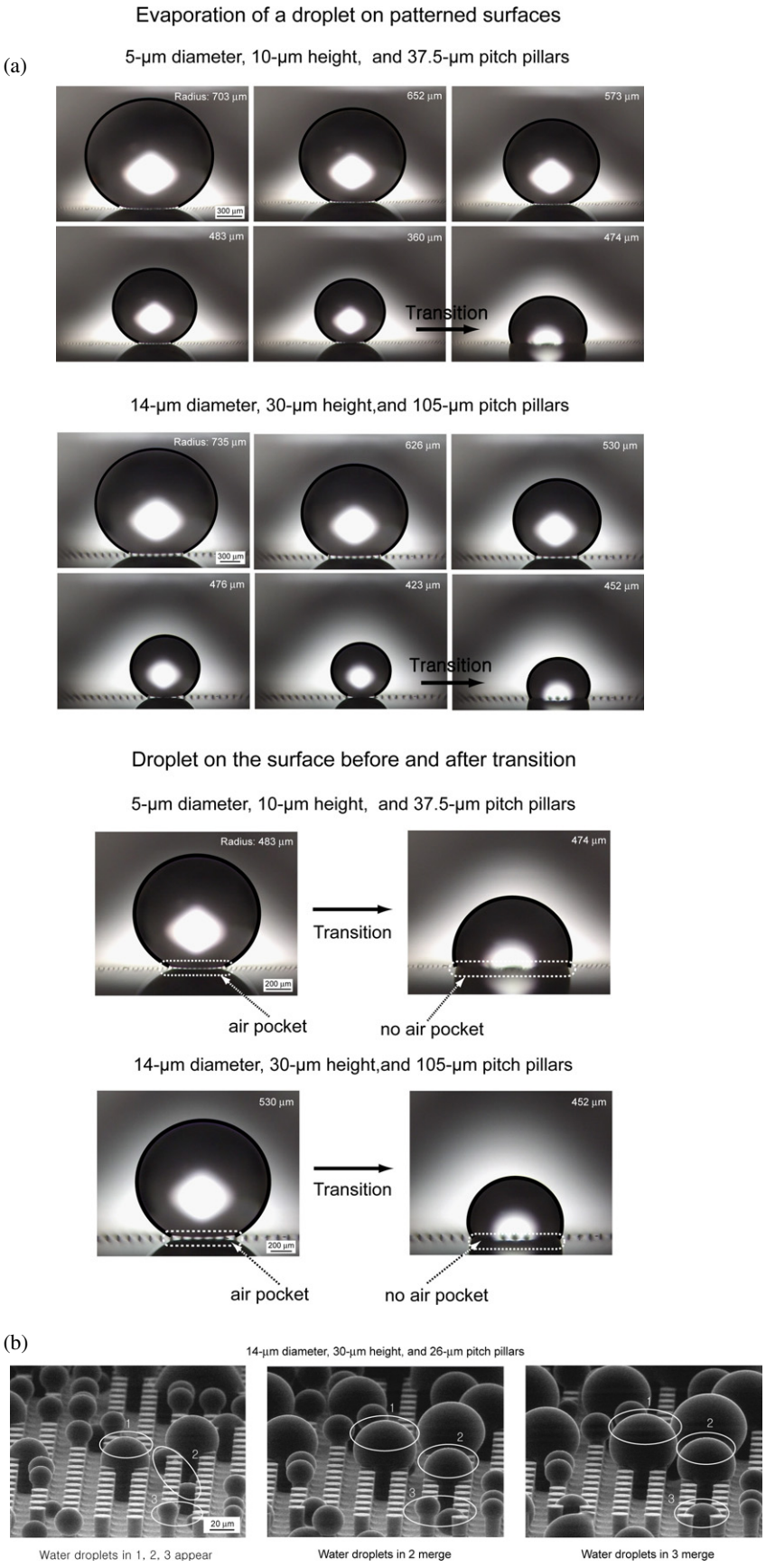

Figure 17. (a) Cassie–Wenzel transition during evaporation, (b) ESEM micrographs of microdroplets which grow and merge during condensation; however, no transition from the Wenzel to the Cassie regime takes place. The Cassie–Wenzel transition is irreversible due to the asymmetry of wetting and dewetting (Jung and Bhushan 2007).

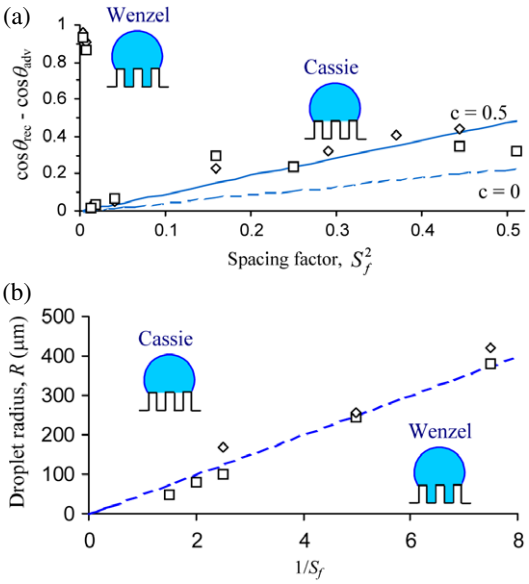

Figure 18. (a) Contact angle hysteresis as a function of S_f for the first (squares) and second (diamonds) series of experiments compared with the theoretically predicted values of $\cos\theta_{adv} - \cos\theta_{rec} = (D/P)^2(\pi/4)(\cos\theta_{adv0} - \cos\theta_{rec0}) + c(D/P)^2$, where c is a proportionality constant. It is observed that when only the adhesion hysteresis/interface energy term is considered ($c = 0$) the theoretical values are underestimated by about a half, whereas $c = 0.5$ provides a good fit. Therefore, the contribution of the adhesion hysteresis is of the same order of magnitude as the contribution of kinetic effects. (b) Droplet radius, R, for the Cassie–Wenzel transition as a function of $P/D = 1/S_f$. It is observed that the transition takes place at a constant value of $RD/P \sim 50$ μm (dashed line). This shows that the transition is a linear phenomenon (Nosonovsky and Bhushan 2007c).

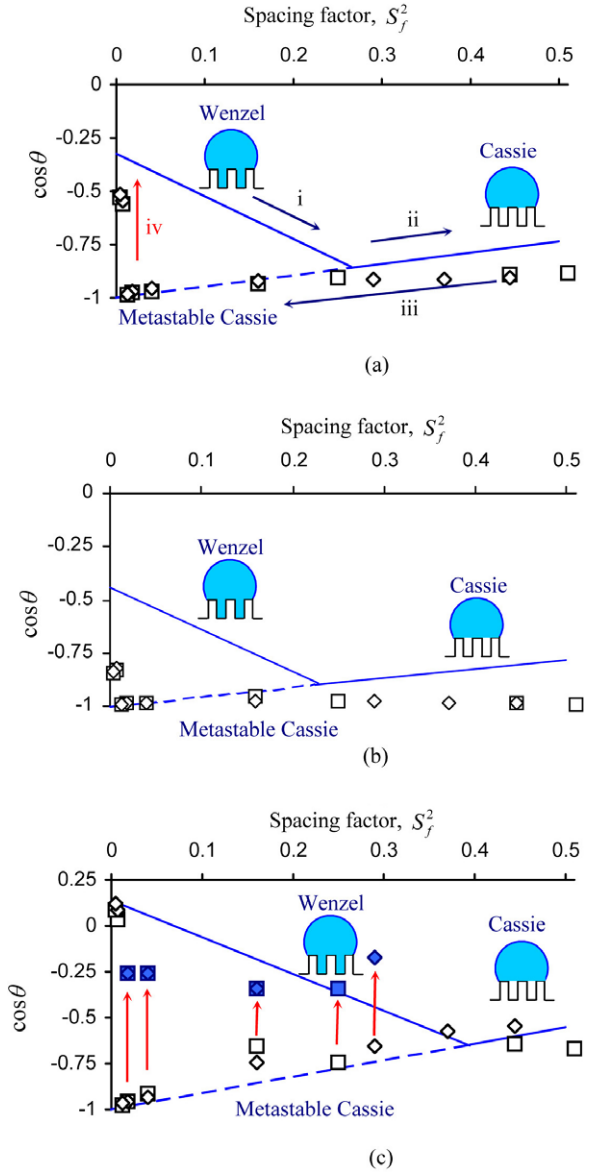

Figure 19. Theoretical (solid and dashed) and experimental (squares for the first series, diamonds for the second series). (a) Contact angle as a function of the spacing factor. (b) Advancing contact angle. (c) Receding contact angle and values of the contact angle observed after the transition during evaporation (shaded) (Nosonovsky and Bhushan 2007c).

it was observed during evaporation in the ESEM. For the both series, the values almost coincided. For comparison, the values of the receding contact angle measured for millimeter-sized water droplets are also shown (squares and diamonds), since evaporation constitutes removal of liquid and thus the contact angle during evaporation should be compared with the receding contact angle. The solid and dashed straight lines correspond to the values of the contact angle, calculated from equations (97) and (98) using the receding contact angle for a nominally flat surface, $\theta_{rec0} = 82°$. Figure 19(c) demonstrates a good agreement between the experimental data and equations (97) and (98).

We showed in the present section that an abrupt transition from the metastable Cassie to the Wenzel wetting regime is found for micropatterned surfaces. The transition can be observed during microdroplet evaporation in the ESEM. The droplet radius at the transition is linearly proportional to the pitch between pillars divided by their diameter. This suggests that interactions at the perimeter of the droplet (rather at the bulk area beneath the droplet) dominate in the transition. We showed also that the transition cannot be predicted from the macroscale equations for the contact angle and the contact angle hysteresis, such as equations (97) and (98), since it involves micro- and nanoscale interactions. We found also that the contact angle hysteresis can be explained as a result of two factors, which act simultaneously. First, the changing contact area affects the hysteresis, since a certain value of the contact angle hysteresis is inherent for even a nominally flat surface. Decreasing the contact area by increasing the pitch between the pillars leads to a proportional decrease of the hysteresis. This effect is clearly proportional to the contact area between the solid surface and the liquid droplet. Second, edges of the pillar tops prevent the motion of the triple line. This roughness effect is proportional to the contact line density and its contribution was, in our experiment, comparable with the contact area effect. Interestingly, the effect of the edges is much more significant for the advancing than for the receding contact angle.

8.3. Discussion

We investigated the Cassie–Wenzel wetting regime transition of micropatterned superhydrophobic surfaces by water droplets and found several effects specific to the multiscale character of this process. First, we discussed applicability of the Wenzel and Cassie equations for average surface roughness and heterogeneity. These equations relate the local contact angle with the apparent contact angle of a rough/heterogeneous surface. However, it is not obvious what should be the size of roughness/heterogeneity averaging, since the triple line, at which the contact angle is defined, has two very different scale lengths: its width is of molecular size scale while its length is of the order of the size of the droplet (that is, microns or millimeters). We presented an argument that in order for the averaging to be valid, the roughness details should be small compared to the size of the droplet (and not the molecular size). We showed that while for the uniform roughness/heterogeneity the Wenzel and Cassie equations can be applied, for a more complicated case of non-uniform heterogeneity, the generalized equations should be used. The proposed generalized Cassie–Wenzel equations are consistent with a broad range of available experimental data. The generalized equations are valid both in the cases when the classical Wenzel and Cassie equations can be applied as well as in the cases when they fail.

The macroscale contact angle hysteresis and Cassie–Wenzel transition cannot be determined from the macroscale equations and are governed by micro- and nanoscale effects, so wetting is a multiscale phenomenon. The kinetic effects associated with the contact angle hysteresis should be studied at the microscale, whereas the effects of the adhesion hysteresis and the Cassie–Wenzel transition involve processes at the nanoscale. Our theoretical arguments are supported by our experimental data on micropatterned surfaces. The experimental study of the contact angle hysteresis demonstrates that two different processes are involved: the changing solid–liquid area of contact and pinning of the triple line. The latter effect is more significant for the advancing than for the receding contact angle. The transition between wetting states was observed for evaporating microdroplets in ESEM and the droplet radius scales well with the geometric parameters of the micropattern. These findings provide new insights into the fundamental mechanisms of wetting and can lead to creation of successful non-adhesive surfaces.

9. Capillary adhesion force due to the meniscus

When two solids come into contact, a meniscus can form due to condensation of liquid or because the liquid film may be present initially, if the liquid is wetting. For non-wetting liquids, meniscus will not be formed. The meniscus causes an increase in the friction force. In this section the effect of surface roughness on the meniscus force will be considered for the case of a sphere in contact with a flat surface (single asperity contact) and for the case of multiple-asperity contact.

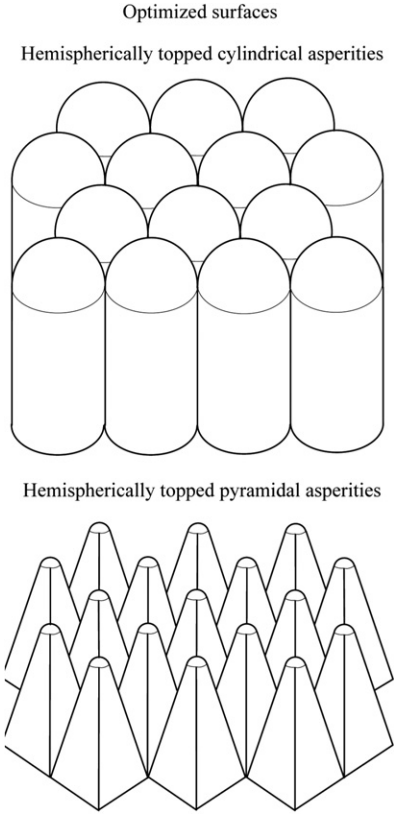

Figure 20. Optimized spaced roughness distribution—hemispherically topped cylindrical asperities and pyramidal asperities with square foundation and rounded tops. A square base gives a higher packing density but introduces undesirable sharp edges (Nosonovsky and Bhushan 2005).

9.1. Sphere in contact with a smooth surface

Consider a sphere with radius R in contact with a flat surface with a meniscus (figure 20(a)). The shape and size of the meniscus, as well as the total energy of the system, depend on the separation distance s between the flat surface and the center of the sphere. The normal meniscus force F_{m}, which acts upon the sphere and the flat surface, can be calculated as the derivative of the energy E_{tot} by s:

$$F_{\mathrm{m}} = \frac{\mathrm{d}E_{\mathrm{tot}}}{\mathrm{d}s}. \tag{99}$$

There are two solid–liquid interfaces, with the sphere and with the flat surface. The areas of these interfaces are approximately equal to πa^2, where a is the meniscus radius. Assuming that the ratio a/R is small and $A_{\mathrm{LA}} \ll A_{\mathrm{SL}}$, the total energy E_{tot} is equal to the sum of the surface energies at the solid–liquid (SL) interface. Based on these assumptions, E_{tot} can be calculated as

$$\begin{aligned} E_{\mathrm{tot}} &= \pi a^2(\gamma_{\mathrm{SL1}} - \gamma_{\mathrm{SA1}} + \gamma_{\mathrm{SL2}} - \gamma_{\mathrm{SA2}}) \\ &= \pi a^2 \gamma_{\mathrm{LA}}(\cos\theta_1 + \cos\theta_2) \end{aligned} \tag{100}$$

where the indices 1 and 2 correspond to the sphere and the flat surface, and a is defined in the figure 20 (Nosonovsky and Bhushan 2005). The volume of liquid V is a function of s and a and is given as the sum of the cylindrical volume with height

$s + a^2/(2R)$ and cross-sectional area πa^2 minus a volume of the spherical segment of height $a^2/(2R)$

$$V = \pi a^2 s + \frac{\pi a^4}{4R}. \tag{101}$$

The volume of the liquid remains constant during the contact, so equation (101) may be viewed as a quadratic equation for a^2, which is solved as

$$a^2 = -2Rs \pm 2R\sqrt{s^2 + V/(\pi R)}. \tag{102}$$

The derivative of a^2 by s, $\mathrm{d}(a^2)/\mathrm{d}s$ for the sphere touching the plane ($s = 0$) is given as

$$\frac{\mathrm{d}a^2}{\mathrm{d}s} = -2R. \tag{103}$$

By using the derivative of equation (100) and the expression in equation (103) in equation (99), we get

$$F_\mathrm{m} = 2\pi R\gamma_\mathrm{LA}(\cos\theta_1 + \cos\theta_2). \tag{104}$$

Equation (104) (also known as equation for the Laplace pressure) provides us with the value of the normal force due to the meniscus. If the sphere and surface are rough, roughness factors of R_f1 and R_f2, respectively, must be taken into account

$$F_\mathrm{m} = 2\pi R\gamma_\mathrm{LA1}(R_\mathrm{f1}\cos\theta_1 + R_\mathrm{f2}\cos\theta_2). \tag{105}$$

In the presence of a meniscus, the friction force is given by Bhushan (1999, 2002).

$$F = \mu(W + F_\mathrm{m}). \tag{106}$$

The coefficient of friction in the presence of the meniscus force, μ_wet, is calculated using only the applied normal load, as usually measured in the experiments

$$\mu_\mathrm{wet} = \mu\left(1 + \frac{F_\mathrm{m}}{W}\right). \tag{107}$$

Equation (107) shows that μ_wet is greater than μ, because F_m is not taken into account for calculation of the normal load in the wet contact.

The effect of meniscus on friction force for different surface roughnesses is presented in figure 20(b). It is observed that a roughness factor of $R_\mathrm{f} = 2$ may result in a significant change in the friction force due to the meniscus. In applications, it is usually desirable to decrease the meniscus forces; therefore, a smooth surface is preferable in the case of single-asperity contact.

9.2. *Multiple-asperity contact*

In the case of multiple-asperity contact, a statistical approach is used to model the contact. For a random surface with a certain σ and β^*, the average peak radius R_p and number of contacts N depend on roughness due to the so-called scale effect (Bhushan and Nosonovsky 2003). Bhushan and Nosonovsky (2004) showed that the average peak radius R_p is related to σ

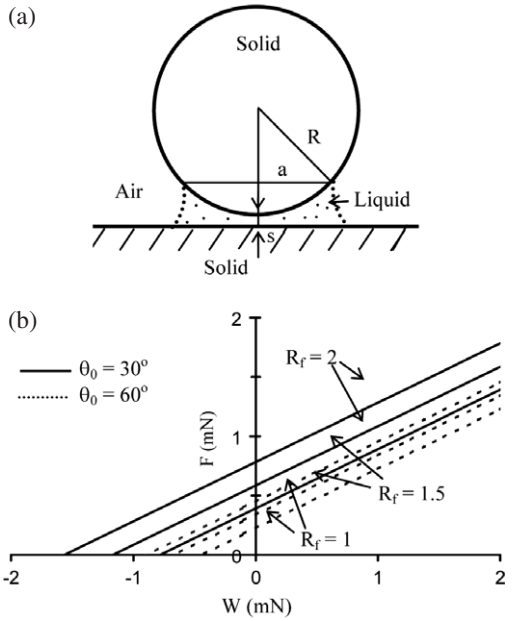

Figure 21. (a) Meniscus formation during wet contact of a flat surface with a sphere. (b) Dependence of the friction force (F) on the normal load (W) for single-asperity contact, $\gamma_\mathrm{LA} = 0.073$ J m^{-2} (water), $R = 1$ mm, $\mu = 0.5$, for different values of $R_\mathrm{f} = R_\mathrm{f1} = R_\mathrm{f2}$, $\theta_0 = \theta_1 = \theta_2$ (Nosonovsky and Bhushan 2005).

and β^*, whereas the number of contacts, for moderate loads, is proportional to the load, divided by σ and β^*

$$R_\mathrm{p} \propto \frac{(\beta^*)^2}{\sigma} \tag{108}$$

$$N \propto \frac{W}{\sigma\beta^*}. \tag{109}$$

For asperities of equal peak radius R_p, the meniscus force is given by Tian and Bhushan (1996), Bhushan (1999, 2002)

$$F_\mathrm{m} = 2\pi R_\mathrm{p}\gamma_\mathrm{LA}(\cos\theta_1 + \cos\theta_2)N \propto \frac{\beta^* W}{\sigma^2}\gamma_\mathrm{LA}(\cos\theta_1 + \cos\theta_2). \tag{110}$$

The size of the menisci is comparable with the size of individual contacts (Nosonovsky and Bhushan 2005).

We consider a rough surface which consists of short-wavelength roughness superimposed over long-wavelength roughness with a typical size of roughness smaller than the meniscus size (figure 21). The nanoscale roughness of the two bodies is characterized by the roughness factors R_f1 and R_f2. We further assume that asperities have an average peak radius $\bar{R}_\mathrm{p}$. Substituting equation (6) into (110) results in

$$F_\mathrm{m} = 2\pi R_\mathrm{p}\gamma_\mathrm{LA}(\cos\theta_1 + \cos\theta_2)N \propto \frac{\beta^* W}{\sigma^2}\gamma_\mathrm{LA}(R_\mathrm{fn1}\cos\theta_1 + R_\mathrm{fn2}\cos\theta_2). \tag{111}$$

The meniscus force as a function of σ^2/β^*, which is a measure of roughness, is presented in figure 22 (Nosonovsky and Bhushan 2005). It is observed that with increasing roughness σ^2/β^*, the meniscus force decreases. A high nanoscale roughness factor may slightly increase the meniscus force.

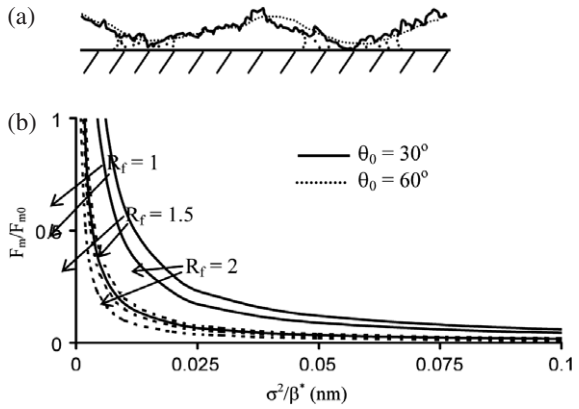

Figure 22. (a) Meniscus formation during wet contact of a smooth surface with a rough surface with a short-wavelength roughness superimposed over long-wavelength roughness (dotted line). (b) Dependence of the meniscus force (normalized by F_{m0}, meniscus force value at $\sigma^2/\beta^* = 0.001$ nm) on roughness σ^2/β^*, for different values of $R_f = R_{f1} = R_{f2}$, $\theta_0 = \theta_1 = \theta_2$ (Nosonovsky and Bhushan 2005).

Since it is usually desirable to reduce the meniscus force, a rough surface with high σ^2/β^* is preferable in the case of multiple-asperity contact (Nosonovsky and Bhushan 2005).

10. Conclusions

We presented here the theory of roughness-induced superhydrophobicity. The Cassie–Baxter and Wenzel equations provide the contact angle with rough and heterogeneous surfaces. The range of applicability of these equations was discussed. We also discussed the contact angle hysteresis and found that it is governed by two factors: the adhesion hysteresis which is inherently present at any surface due to the nanoscale roughness or heterogeneity and the kinetic effects related to pinning of the triple line. Two wetting regimes are possible: the homogeneous (Wenzel) regime and the composite (Cassie) regime with air bubbles trapped between the solid and liquid. For practical applications, the composite regime is required, because it results in low contact angle hysteresis and, therefore, low rates of dissipation and low adhesion, as well as in a high contact angle. The transition between the Cassie and Wenzel regimes for micropatterned superhydrophobic surfaces was discussed. While the exact micro- and nanoscale mechanism of this transition is still not clear, the experimental data suggest that simple microscale geometrical parameters control this transition.

Wetting of a micropatterned surface is a complicated process that involves process at several scale levels. While the macroscale parameters such as the contact angle and contact angle hysteresis may be governed approximately by macroscale equations, such as equations (5)–(10), these equations do not provide a complete description of the macroscale behavior of a system. The contact angle hysteresis is dependent upon micro- and nanoscale effects that control energy dissipation due to the adhesion, kinetic effects and the fine structure of the triple line. The Cassie–Wenzel wetting state transition is also governed by these micro- and nanoscale effects as well as by dynamic effects such as capillary waves. Furthermore, the very concept of the contact angle is relevant only at the macroscale, and to some extent at the microscale, while at the lower scale such effects as layer and precursor formation, disjoining pressure, surface heterogeneity, contact line tension, and a finite thickness of the liquid–vapor interface dominate. Therefore, despite its apparent simplicity, a droplet upon a rough surface constitutes a multiscale system. In order to control wetting, it is necessary to control parameters at different scale levels. It is not surprising that biological superhydrophobic surfaces have roughnesses at different scale lengths.

Water-repellent non-adhesive surfaces are required for many tribological applications. We discussed the dependence of the meniscus force, which is often the principal component of the friction force, upon roughness.

References

Adamson A V 1990 *Physical Chemistry of Surfaces* (New York: Wiley)
Anisimov M A 2007 Divergence of Tolman's length for a droplet near the critical point *Phys. Rev. Lett.* **98** 035702
Bahadur V and Garimella S V 2007 Electrowetting-based control of static droplet states on rough surfaces *Langmuir* **23** 4918–24
Barbieri L, Wagner E and Hoffmann P 2007 Water wetting transition parameters of perfluorinated substrates with periodically distributed flat-top microscale obstavles *Langmuir* **23** 1723–34
Bartell F E and Shepard J W 1953 Surface roughness as related to hysteresis of contact angles *J. Phys. Chem.* **57** 455–8
Barthlott W and Neinhuis C 1997 Purity of the sacred lotus, or escape from contamination in biological surfaces *Planta* **202** 1–8
Bhushan B 1998 *Tribology Issues and Opportunities in MEMS* (Dordrecht: Kluwer–Academic)
Bhushan B 1999 *Principles and Applications of Tribology* (New York: Wiley)
Bhushan B 2002 *Introduction to Tribology* (New York: Wiley)
Bhushan B 2003 Adhesion and stiction: mechanisms, measurement techniques and methods for reduction *J. Vac. Sci. Technol.* B **21** 2262–96
Bhushan B 2005 *Nanotribology and Nanomechanics—An Introduction* (Heidelberg: Springer)
Bhushan B 2007 *Springer Handbook of Nanotechnology* 2nd edn (Heidelberg: Springer)
Bhushan B and Jung Y C 2006 Micro and nanoscale characterization of hydrophobic and hydrophilic leaf syrface *Nanotechnology* **17** 2758–72
Bhushan B and Jung Y C 2007 Wetting study of patterned surfaces for superhydrophobicity *Ultramicroscopy* **107** 1033–41
Bhushan B, Israelachvili J N and Landman U 1995 Nanotribology: friction, wear and lubrication at the atomic scale *Nature* **374** 607–16
Bhushan B and Nosonovsky M 2003 Scale effects in friction using strain gradient plasticity and dislocation-assisted sliding (microslip) *Acta Mater.* **51** 4331–45
Bhushan B and Nosonovsky M 2004 Scale effects in dry and wet friction, wear, and interface temperature *Nanotechnology* **15** 749–61
Bhushan B, Nosonovsky M and Jung Y C 2007 Towards optimization of patterned superhydrophobic surfaces *J. R. Soc. Interface* **4** 643–8
Bico J, Thiele U and Quéré D 2002 Wetting of textured surfaces *Colloids Surf.* A **206** 41–6
Bormashenko E, Pogreb R, Whyman G and Erlich M 2007 Cassie–Wenzel wetting transition in vibrated drops deposited on the rough surfaces: is dynamic Cassie–Wenzel transition 2D or 1D affair? *Langmuir* **23** 6501–3

Burton Z and Bhushan B 2005 Hydrophobicity, adhesion, and friction properties of nanopatterned polymers and scale dependence for micro- and nanoelectromechanical systems *Nano Lett.* **5** 1607–13
Burton Z and Bhushan B 2006 Surface characterization and adhesion and friction properties of hydrophobic leaf surfaces *Ultramicroscopy* **106** 709–19
Cassie A and Baxter S 1944 Wettability of porous surfaces *Trans. Faraday Soc.* **40** 546–51
Checco A, Guenoun P and Daillant J 2003 Nonlinear dependence of the contact angle of nanodroplets on contact line curvatures *Phys. Rev. Lett.* **91** 186101
Cheng Y T, Rodak D E, Angelopoulos A and Gacek T 2005 Microscopic observation of condensation of water on lotus leaves *Appl. Phys. Lett.* **87** 194112
Craig R G, Berry G C and Peyton F A 1960 Wetting of poly-(methyl methacrylate) and polystyrene by water and saliva *J. Phys. Chem.* **64** 541–3
de Gennes P G, Brochard-Wyart F and Quėrė D 2003 *Capillarity and Wetting Phenomena* (Berlin: Springer)
Derjaguin B V and Churaev N V 1974 Structural component of disjoining pressure *J. Colloid Interface Sci.* **49** 249–55
Eustathopoulos N, Nicholas M G and Drevet B 1999 *Wettability at High Temperatures* (Amsterdam: Pergamon)
Erbil H Y, Demirel A L and Avci Y 2003 Transformation of a simple plastic into a superhydrophobic surface *Science* **299** 1377–80
Extrand C W 2002 Model for contact angle and hysteresis on rough and ultraphobic surfaces *Langmuir* **18** 7991–9
Extrand C W 2003 Contact Angle hysteresis on surfaces with chemically heterogeneous islands *Langmuir* **19** 3793–6
Eyring H 1964 *Statistical Mechanics and Dynamics* (New York: Wiley)
Feng X J, Feng L, Jin M H, Zhai J, Jiang L and Zhu D B 2004 Reversible super-hydrophobicity to super-hydrophilicity transition of aligned ZnO nanorod films *J. Am. Chem. Soc.* **126** 62–3
Feng L, Li S, Li Y, Li H, Zhang L, Zhai J, Song Y, Liu B, Jiang L and Zhu D 2002 Super-hydrophobic surfaces: from natural to artificial *Adv. Mater.* **14** 1857–60
Gao X F and Jiang L 2004 Biophysics: water-repellent legs of water striders *Nature* **432** 36
Gao L and McCarthy T J 2006 The lotus effect explained: two reasons why two length scales of topography are important *Langmuir* **22** 2966–7
Gao L and McCarthy T J 2007 How Wenzel and Cassie were wrong *Langmuir* **23** 3762–5
Greenberg M D 1978 *Foundation of Applied Mathematics* (Englewood Cliffs, NJ: Prentice-Hall)
Gupta P, Ulman A, Fanfan F, Korniakov A and Loos K 2005 Mixed self-assembled monolayer of alkanethiolates on ultrasmooth gold do not exhibit contact angle hysteresis *J. Am. Chem. Soc.* **127** 4–5
He B, Patankar N A and Lee J 2003 Multiple equllibrium droplet shapes and design criterion for rough hydrophobic surfaces *Langmuir* **19** 4999–5003
Herminghaus S 2000 Roughness-induced non-wetting *Europhys. Lett.* **52** 165–70
Ishino C and Okumura K 2006 Nucleation scenarios for wetting transition on textured surfaces: the effect of contact angle hysteresis *Europhys. Lett.* **76** 464–70
Israelachvili J N 1992 *Intermolecular and Surface Forces* 2nd edn (London: Academic)
Israelachvili J N and Gee M L 1989 Contact angles on chemically heterogeneous surfaces *Langmuir* **5** 288–9
Johnson R E and Dettre R H 1964 Contact angle hysteresis *Contact Angle, Wettability, and Adhesion, Adv. Chem. Ser.* vol 43, ed F M Fowkes (Washington, DC: American Chemical Society) pp 112–35
Jung Y C and Bhushan B 2006 Contact angle, adhesion, and friction properties of micro- and nanopetterned polymers for superhydrophobicity *Nanotechnology* **17** 4970–80
Jung Y C and Bhushan B 2007 Wetting behavior during evaporation and condensation of water microdroplets on superhydrophobic patterned surfaces *J. Microsc.* at press
Kamusewitz H, Possart W and Paul D 1999 The relation between Young's equilibrium contact angle and the hysteresis on rough paraffin wax surfaces *Colloids Surf.* A **156** 271–9
Kijlstra J, Reihs K and Klami A 2002 Roughness and topology of ultra-hydrophobic surfaces *Colloids Surf.* A **206** 521–9
Krasovitski B and Marmur A 2004 Drops down the hill: theoretical study of limiting contact angles and the hysteresis range on a tilted plane *Langmuir* **21** 3881–5
Krupenkin T N, Taylor J A, Schneider T M and Yang S 2004 From rolling ball to complete wetting: the dynamic tuning of liquids on nanostructured surfaces *Langmuir* **20** 3824–7
Lafuma A and Quėrė D 2003 Superhydrophobic states *Nat. Mater.* **2** 457–60
Landau L and Lifshitz E 1959 *Fluid Mechanics* (London: Pergamon)
Li W and Amirfazli A 2006 A thermodynamic approach for determining the contact angle hysteresis for superhydrophobic surfaces *J. Colloid Interface Sci.* **292** 195–201
Marmur A 2003 Wetting on hydrophobic rough surfaces: to be heterogeneous or not to be? *Langmuir* **19** 8343–8
Marmur A 2004 The lotus effect: superhydrophobicity and metastability *Langmuir* **20** 3517–9
Miwa M, Nakajima A, Fujishima A, Hashimoto K and Watanabe T 2000 Effects of the surface roughness on sliding angles of water droplets on superhydrophobic surfaces *Langmuir* **16** 5754–60
Neinhuis C and Barthlott W 1997 Characterization and distribution of water-repellent, self-cleaning plant surfaces *Ann. Botany* **79** 667–77
Nosonovsky M 2007a Multiscale roughness and stability of superhydrophobic biomimetic interfaces *Langmuir* **23** 3157–61
Nosonovsky M 2007b Model for solid–liquid and solid–solid friction for rough surfaces with adhesion hysteresis *J. Chem. Phys.* **126** 224701
Nosonovsky M 2007c On the range of applicability of the Wenzel and Cassie equations *Langmuir* **23** 9919–20
Nosonovsky M and Bhushan B 2005 Roughness optimization for biomimetic superhydrophobic surfaces *Microsyst. Technol.* **11** 535–49
Nosonovsky M and Bhushan B 2006a Stochastic model for metastable wetting of roughness-induced superhydrophobic surfaces *Microsyst. Technol.* **12** 231–7
Nosonovsky M and Bhushan B 2006b Wetting of rough three-dimensional superhydrophobic surfaces *Microsyst. Technol.* **12** 273–81
Nosonovsky M and Bhushan B 2007a Hierarchical roughness makes superhydrophobic surfaces stable *Microelectron. Eng.* **84** 382–6
Nosonovsky M and Bhushan B 2007b Hierarchical roughness optimization for biomimetic superhydrophobic surfaces *Ultramicroscopy* **107** 969–79
Nosonovsky M and Bhushan B 2007c Biomimetic superhydrophobic surfaces: multiscale approach *Nano Lett.* **7** 2633–7
Onda T, Shibuichi S, Satoh N and Tsujii K 1996 Super-water-repellent fractal surfaces *Langmuir* **12** 2125–7
Oner D and McCarthy T J 2000 Ultrahydrophobic surfaces. Effects of topography length scales on wettability *Langmuir* **16** 7777–82
Pompe T, Fery A and Herminghaus S 2000 Measurement of contact line tension by analysis of the three-phase boundary with nanometer resolution *Apparent and Microscopic Contact Angles* ed J Drelich, J S Laskowski and K L Mittal (Utrecht: VSP) pp 3–12

Patankar N A 2003 On the modeling of hydrophobic contact angles on rough surfaces *Langmuir* **19** 1249–53
Patankar N A 2004a Transition between superhydrophobic states on rough surfaces *Langmuir* **20** 7097–102
Patankar N A 2004b Mimicking the lotus effect: influence of double roughness structures and slender pillars *Langmuir* **20** 8209–13
Quéré D 2005 Non-sticking drops *Rep. Prog. Phys.* **68** 2495–535
Satas D (ed) 1991 *Coating Technology Handbook* (New York: Dekker)
Semal S, Blake T D, Geskin V, de Ruijter M L, Castelein G and De Coninck J 1999 Influence of surface roughness on wetting dynamics *Langmuir* **15** 8765–70
Sharma R and Ross D S 1991 Kinetics of liquid penetration into periodically constrained capillaries *J. Chem. Soc. Faraday Trans.* **87** 619–24
Shibuichi S, Onda T, Satoh N and Tsujii K 1996 Super-water-repellent surfaces resulting from fractal structure *J. Phys. Chem.* **100** 19512–7
Shuttleworth R and Bailey G L J 1948 The spreading of a liquid over a rough solid *Discuss. Faraday Soc.* **3** 16–22
Sun M, Luo C, Xu L, Ji H, Ouyang Q, Yu D and Chen Y 2005 Artificial lotus leaf by nanocasting *Langmuir* **21** 8978–81
Tian X and Bhushan B 1996 The micro-meniscus effect of a thin liquid film on the static friction of rough surface contact *J. Phys. D: Appl. Phys.* **29** 163–78
Tretinnikov O N 2000 Wettability and microstructute of polymer surfaces: stereochemical and conformational aspects *Apparent and Microscopic Contact Angles* ed J Drelich, J S Laskowski and K L Mittal (Utrecht: VSP) pp 111–28
Tsori Y 2006 Discontinuous liquid rise in capillaries with varying cross-sections *Langmuir* **22** 8860–3
Wagner P, Furstner R, Barthlott W and Neinhuis C 2003 Quantitative assessment to the structural basis of water repellency in natural and technical surfaces *J. Exp. Botany* **54** 1295–303
Wang S, Feng L and Jiang L 2006 One-step solution-immersion process for the fabrication of stable bionic superhydrophobic surfaces *Adv. Mater.* **18** 767–70
Wenzel R N 1936 Resistance of solid surfaces to wetting by water *Ind. Eng. Chem.* **28** 988–94
Whitehouse D J and Archard J F 1970 The properties of random surfaces of significance in their contact *Proc. R. Soc.* A **316** 97–121
Yost F G, Michael J R and Eisenmann E T 1995 Extensive wetting due to roughness *Acta Metall. Mater.* **45** 299–305
Zhou X B and De Hosson J Th M 1995 Influence of surface roughness on the wetting angle *Acta Metall. Mater.* **45** 299–305